Time-dependent MHD modeling of the global solar corona for year 2007: Driven by daily-updated magnetic field synoptic data

L. P. Yang,[1] X. S. Feng,[1] C. Q. Xiang,[1] Yang Liu,[2] Xuepu Zhao,[2] and S. T. Wu[3]

Received 29 December 2011; revised 14 June 2012; accepted 4 July 2012; published 28 August 2012.

[1] In this paper, we develop a time-dependent MHD model driven by the daily-updated synoptic magnetograms (MHD-DUSM) to study the dynamic evolution of the global corona with the help of the 3D Solar-Interplanetary (SIP) adaptive mesh refinement (AMR) space-time conservation element and solution element (CESE) MHD model (SIP-AMR-CESE MHD Model). To accommodate the observations, the tangential component of the electric field at the lower boundary is specified to allow the flux evolution to match the observed changes of magnetic field. Meanwhile, the time-dependent solar surface boundary conditions derived from the method of characteristics and the mass flux limit are incorporated to couple the observation and the 3D MHD model. The simulated evolution of the global coronal structure during 2007 is compared with solar observations and solar wind measurements from both Ulysses and spacecrafts near the Earth. The MHD-DUSM model is also validated by comparisons with the standard potential field source surface (PFSS) model, the newly improved Wang-Sheeley-Arge (WSA) empirical formula, and the MHD simulation with a monthly synoptic magnetogram (MHD-MSM). Comparisons show that the MHD-DUSM results have good overall agreement with coronal and interplanetary structures, including the sizes and distributions of coronal holes, the positions and shapes of the streamer belts, and the transitions of the solar wind speeds and magnetic field polarities. The MHD-DUSM results also display many features different from those of the PFSS, the WSA, and the MHD-MSM models.

Citation: Yang, L. P., X. S. Feng, C. Q. Xiang, Y. Liu, X. Zhao, and S. T. Wu (2012), Time-dependent MHD modeling of the global solar corona for year 2007: Driven by daily-updated magnetic field synoptic data, *J. Geophys. Res.*, *117*, A08110, doi:10.1029/2011JA017494.

1. Introduction

[2] The solar coronal magnetic field, the cause of the most spectacular phenomena in the heliosphere, plays a crucial role in determining the structure of the solar corona, such as the shapes, positions, and sizes of the coronal streamers and the coronal holes. Since direct measurements of the coronal magnetic field [*Judge*, 1998; *Lin et al.*, 2000; *Tomczyk et al.*, 2008; *Petrie and Patrikeeva*, 2009] are difficult to carry out, global corona magnetic field is usually based on extrapolations from line-of-sight (LOS) magnetic field on the photospheric surface, which has been routinely measured for many years from both the ground-based observations (e.g., Stanford's Wilcox Solar Observatory (WSO), the National Solar Observatory at Kitt Peak, the Mount Wilson Observatory, the Global Oscillations Network (GONG) and the Nobeyama Solar Radio Observatory) and the space-borne instruments (e.g., the Michelson Doppler Imager (MDI) aboard the Solar Heliospheric Observatory (SOHO) as well as recently from Helioseismic and Magnetic Imager (HMI) aboard Solar Dynamics Observatory (SDO)).

[3] Based on the photospheric magnetic field measurements, two types of approaches have been established to extrapolate the coronal magnetic field according to whether the effects of the pressure gradient and the gravitational force of the coronal plasma are taken into account or not. One type of methods includes the models of nonlinear force-free field and the method of potential field source surface (PFSS) and the other is the global magnetohydrodynamics (MHD) simulation.

[4] The first class of methods assumes that the force-free magnetic field is generally applicable in the region between the base of the corona and two or three solar radii above the photosphere because the magnetic field predominates over the thermal pressure gradient of the expanding solar wind and the gravitational force. This kind of methods reduces to solve the following set of equations

$$\nabla \times \mathbf{B} = \alpha(\mathbf{x})\mathbf{B}, \tag{1}$$

$$\nabla \cdot \mathbf{B} = 0, \tag{2}$$

[1]SIGMA Weather Group, State Key Laboratory of Space Weather, Center for Space Science and Applied Research, Chinese Academy of Sciences, Beijing, China.
[2]W.W. Hansen Experimental Physics Laboratory, Stanford University, Stanford, California, USA.
[3]Center for Space Plasma and Aeronomic Research, University of Alabama in Huntsville, Huntsville, Alabama, USA.

Corresponding author: L. P. Yang, SIGMA Weather Group, State Key Laboratory of Space Weather, Center for Space Science and Applied Research, Chinese Academy of Sciences, Beijing 100190, China. (lpyang@spaceweather.ac.cn)

0148-0227/12/2011JA017494

where **B** is the magnetic flux density and $\alpha(\mathbf{x})$ is a function of space and must be a constant along the field lines defined by equation (2).

[5] Several numerical codes have been proposed to derive nonlinear force-free fields in the active regions from the photospheric vector magnetic field measurements, such as the Grad-Rubin method [*Grad and Rubin*, 1958; *Sakurai*, 1981; *Song et al.*, 2006, 2007], the upward integration method [*Nakagawa*, 1974; *Wu et al.*, 1985, 1990a, 1990b], the MHD relaxation method [*Chodura and Schlueter*, 1981; *Mikić and McClymont*, 1994], the optimization approach [*Wheatland et al.*, 2000] and the boundary element method [*Yan and Sakurai*, 2000; *Yan and Li*, 2006]. Recently, *Wiegelmann* [2007] and *Wiegelmann* [2008] described newly developed code for the extrapolation of nonlinear force-free coronal magnetic fields in spherical coordinates by using the measured vector magnetograms on the solar photosphere as input and solving the force-free equations in the low-latitude region of solar corona. *Contopoulos et al.* [2011] presented a novel numerical method that allows the calculation of nonlinear force-free magnetostatic solutions above a boundary surface on which only the distribution of the normal magnetic field component is given. *Ruan et al.* [2008] established a magnetohydrostatic nonlinear force-free model for the global corona, which could be compared directly with observations. Inserting the observations of the new active regions into the simulations governed by the reduced MHD equations, *Yeates et al.* [2007, 2008, 2010] and *Yeates and Mackay* [2009] constructed a continuous sequence of quasi-static nonlinear force-free fields for the global corona in response to flux emergence and shearing by the large-scale surface motions.

[6] In fact, $\alpha(\mathbf{x})$ in equation (1) is inversely proportional to the characteristic length scale of the investigated structure. Therefore, for the study of the coronal large-scale structures, it is often assumed that there is no significant current in the solar corona [*Petrie et al.*, 2008]. Under this assumption, researchers have developed several models such as the potential field source surface (PFSS) model [*Schatten et al.*, 1969; *Altschuler and Newkirk*, 1969; *Schatten*, 1971], Schatten current sheet (SCS) model [*Schatten et al.*, 1969; *Schatten*, 1971] and horizontal-current current-sheet source surface (HCCSSS) model [*Zhao and Hoeksema*, 1994, 1995, 2010]. Among them, the HCCSS model considers the effects of streamer current sheets and uses horizontal electric current in the lower corona as a free parameter. These magnetic field models have been used in the WSA model [*Arge and Pizzo*, 2000; *Arge et al.*, 2003; *Owens et al.*, 2005, 2008; *McGregor et al.*, 2008, 2011a, 2011b; *Sun et al.*, 2011] to predict the background solar wind speed and the interplanetary magnetic field (IMF) polarity from photospheric observation. The PFSS model has also been widely used in the study of the large-scale coronal and heliospheric structures [e.g., *Smith and Schatten*, 1970; *Burlaga et al.*, 1978; *Neugebauer et al.*, 2002; *Riley et al.*, 2006].

[7] The other kind of models for studying these topics is the global MHD model, which was developed almost 40 years ago [*Pneuman and Kopp*, 1971; *Endler*, 1971]. The advantages of this approach are that no assumptions are made about the nature of coronal currents or other properties, and the nonlinear interactions between the plasma and magnetic field in the sub-Alfvénic solar corona and the super-Alfvénic interplanetary space can be self-consistently treated [*Linker et al.*, 1999; *Lionello et al.*, 2006; *Hayashi et al.*, 2008]. Currently, most of MHD models of the global solar corona and solar wind employ the measured or synthetic data of the solar photospheric magnetic field as the bottom boundary conditions [e.g., *Usmanov*, 1993; *Mikić et al.*, 1999; *Linker et al.*, 1999; *Riley et al.*, 2001; *Roussev et al.*, 2003; *Hayashi*, 2005; *Wu et al.*, 2006; *Hayashi et al.*, 2006; *Cohen et al.*, 2007, 2008; *Feng et al.*, 2007; *Hu et al.*, 2008; *Hayashi et al.*, 2008; *Lionello et al.*, 2009; *Wu et al.*, 2009; *Nakamizo et al.*, 2009; *van der Holst et al.*, 2010; *Feng et al.*, 2010; *Wang et al.*, 2011; *Feng et al.*, 2011a, 2012; *Yang et al.*, 2011]. In addition, other MHD simulations use observational data of density, temperature and velocity on the solar surface for a specified Carrington Rotation (CR) besides the solar photospheric magnetic field to prescribe the plasma parameters on the bottom boundary [e.g., *Hayashi et al.*, 2006; *van der Holst et al.*, 2010; *Wang et al.*, 2011]. For a survey of solar wind modeling, refer to *Feng et al.* [2011b].

[8] Usually, researchers initialize the MHD codes by using potential magnetic field based on the synoptic charts constructed from the line-of-sight measurements of the photospheric magnetic field and Parker solar wind solution to run in time-relaxation method until a steady-state equilibrium is achieved. The concept of a synoptic chart was drawn for each rotation by *Bumba and Howard* [1965], which assumes that the photospheric magnetic field in a global scale is stable during one CR period and that the solar differential rotation can be neglected. Because the Sun rotates $\sim$13° per day as viewed from the Earth, magnetograms taken on consecutive days differ in their central meridian longitudes by $\sim$13° to $\sim$15° depending on the exact time of observation. A synoptic daily are constructed as follows. Daily magnetograms are used by overlaying them and for overlapping regions a weighted average is employed with the weighting factor as a function of longitudinal distance and sharply peaking at the location of the Sun's central meridian at the time of observation [*Arge and Pizzo*, 2000]. By the time the following edges of subsequent magnetograms have rotated beyond the longitude of each cell, there are up to $\sim$16 individual observations weighted together to constitute each cell on a synoptic map. However, X. P. Zhao et al. (The synchronic frame of photospheric magnetic flux: The improved synoptic frame, unpublished manuscript, 2011) pointed out that a limitation of these charts is that each Carrington longitude is observed at a different time. Due to the availability of the data only near central meridian from each magnetogram, the constructed synoptic chart does not have sufficient information at the particular time in the specified CR. However, to use the most recent observations and to specify the solar surface magnetic field at a particular region and a particular time of interest seem helpful to discuss a particular event [*Hayashi et al.*, 2008].

[9] The improved version of synoptic charts is due to the daily-updated magnetic field synoptic charts comprised by the most recent 360° of observations and begin with the leading edge of the most recent magnetogram [*Arge and Pizzo*, 2000]. Unlike the traditional synoptic charts mentioned above, daily-updated synoptic charts are based on the fewer averaged magnetograms. In fact, the 10°$\sim$15° of longitude around the most recent magnetogram's central meridian are often directly added to the daily-updated

synoptic charts without weighted mean. For the most recent magnetic data on the maps, the fewest number of observations are used. Therefore, daily-updated maps are much more sensitive to the quality of the individual magnetograms although the solar magnetic field measurement can be best done for the meridional bin on the solar disc. One advantage of the daily-updated synoptic charts is that the most recent magnetic observations always contain the part of the charts directed towards Earth. Another is that we can employ the most recent magnetic observations to drive models, which allows the models to keep pace with changes in the magnetic field configuration on a timescale of the order 1 day. *Arge and Pizzo* [2000] have used the daily-updated magnetic field synoptic charts to predict the background solar wind speed and interplanetary magnetic field (IMF) polarity, which give better results than the traditional synoptic charts and improve the performance and reliability of the WSA model.

[10] It should be pointed out that the MHD modeling for the solar corona and solar wind is essentially time-independent, which integrate the MHD equations to obtain a steady-state solution by the time-relaxation method. The implicit assumption in the synoptic chart-based MHD models is that the evolution of the field is quasi-steady and the evolution can be approximated by a sequence of steady states [*Lepri et al.*, 2008]. To validate the quasi-steady approximation, the photospheric magnetic fields are supposed to evolve slowly compared to the timescale for establishing a steady solution. However, it is well known that even during solar minimum, the photospheric field is always evolving and at solar maximum period, it can change drastically over a Carrington rotation. Also, the time history of the coronal field is neglected in calculating its structure. Another disadvantage about the quasi-steady assumption is that MHD model results can not simultaneously responds to the dynamic or time-dependent evolution of the global corona. In fact, even the basic processes that produce the ambient solar wind or occur in it are controlled by intrinsically time-dependent processes [*Riley et al.*, 2006]. Therefore, in this paper we try to perform MHD simulation driven by daily-updated magnetic field synoptic magnetograms (MHD-DUSM) to investigate the evolution of the large-scale coronal structure in the year of 2007. In what follows, a general description of the SIP-AMR-CESE MHD model [*Feng et al.*, 2012] is briefly provided in section 2. Then, we present the treatments of the solar surface boundary. Section 4 will show the simulation results, which are compared with the synoptic and daily observations, the interplanetary measurements by mapping Ulysses' observation and OMNI data back into the computational domain, and the MHD model driven by a monthly synoptic magnetogram (MHD-MSM). The last section is reserved for conclusions and discussions.

2. The 3D SIP-AMR-CESE MHD Model

[11] By splitting the magnetic field, the basic equations governing the system are the set of the ideal MHD equations in the conservative form written as follows:

$$\frac{\partial \mathbf{U}}{\partial t} + \nabla \cdot \mathbf{F} = \mathbf{S} \tag{3}$$

where

$$\mathbf{U} = (\rho, \rho\mathbf{u}, e_1, \mathbf{B})^T$$

with a flux tensor $\mathbf{F}$ having the following form

$$\mathbf{F} = \begin{pmatrix} \rho\mathbf{u} \\ \rho\mathbf{u}\mathbf{u} + \mathbf{I}\left(p + \frac{1}{2}\mathbf{B}_1^2 + \mathbf{B}_1 \cdot \mathbf{B}_0\right) - \mathbf{B}_1\mathbf{B}_1 - \mathbf{B}_1\mathbf{B}_0 - \mathbf{B}_0\mathbf{B}_1 \\ \mathbf{u}\left(e_1 + p + \frac{1}{2}\mathbf{B}_1^2 + \mathbf{B}_1 \cdot \mathbf{B}_0\right) - (\mathbf{u} \cdot \mathbf{B}_1)(\mathbf{B}_1 + \mathbf{B}_0) \\ \mathbf{u}\mathbf{B} - \mathbf{B}\mathbf{u} \end{pmatrix}$$

and the source term $\mathbf{S}$ taken as

$$\mathbf{S} = (0, \rho\mathbf{F}_0, \rho\mathbf{u} \cdot \mathbf{F}_0, 0)^T - \nabla \cdot \mathbf{B}(0, \mathbf{B}, \mathbf{u} \cdot \mathbf{B}, \mathbf{u})^T + (0, \mathbf{0}, 0, \nabla(\mu\nabla \cdot \mathbf{B}))^T + (0, \mathbf{0}, Q_e, \mathbf{0})^T$$

Here, ρ is the mass density; $\mathbf{u} = (u, v, w)$ are the velocities in x, y, and z directions; p is the thermal pressure; $\mathbf{B}$, $\mathbf{B}_0$, and $\mathbf{B}_1$ denote the total magnetic field, the potential magnetic field and the perturbed component such that $\mathbf{B} = \mathbf{B}_0 + \mathbf{B}_1$. γ is the specific heat ratio and is taken to be 1.5 here. e_1 corresponds to the modified total energy density consisting of the kinetic energy density, thermal energy density, and magnetic energy density written in terms of $\mathbf{B}_1$, which is equivalent to $e_1 = \frac{1}{2}\rho\mathbf{u}^2 + \frac{p}{\gamma - 1} + \frac{1}{2}\mathbf{B}_1^2$. t and $\mathbf{r}$ is time and position vector originating at the center of the Sun. $\mathbf{F}_1$ is the external force exerted on the plasma. In the source term, the external force $\mathbf{F}_0 = -\frac{GM_s}{r^3}\mathbf{r} - \boldsymbol{\Omega} \times (\boldsymbol{\Omega} \times \mathbf{r}) - 2\boldsymbol{\Omega} \times \mathbf{u}$ is the sum of solar gravity force and inertial force due to the corotating frame with the Sun. G, M_s, and Ω are the gravity constant, solar mass and solar angular speed.

[12] At the same time, Powell's source terms $-\nabla \cdot \mathbf{B}(0, \mathbf{B}, \mathbf{u} \cdot \mathbf{B}, \mathbf{u})^T$ [*Powell et al.*, 1999] and diffusive control term $\nabla(\mu\nabla \cdot \mathbf{B})$ [*Marder*, 1987; *Dedner et al.*, 2002; *Mignone and Tzeferacos*, 2010] have been added in the MHD equations to deal with the divergence of magnetic field. The viscous fluxes $\mu\nabla \cdot \mathbf{B}$ to the magnetic induction equation is properly chosen to maximize the diffusion without introducing a numerical instability, and in our computation, we use $\mu = C_d\left(\frac{1}{\Delta r^2} + \frac{1}{(r\Delta\theta)^2} + \frac{1}{(rsin(\theta)\Delta\phi)^2}\right)^{-1}$ with $C_d = 1.3$, where Δr, $r\Delta\theta$ and $r\sin(\theta)\Delta\phi$ are grid spacings in spherical coordinates [*Feng et al.*, 2012].

[13] The primitive variables ρ, $\mathbf{u}$, p, $\mathbf{B}$, r, and t in these equations are normalized by the characteristic values ρ_S, a_S, $\rho_S a_S^2\sqrt{\rho_S a_S^2}$, R_S, and R_S/a_S, where ρ_S and a_S are the density and ion-acoustic wave speed at the solar surface of one solar radius R_S. The solar rotation is considered in the present study with angular velocity $|\boldsymbol{\Omega}| = 2\pi/27.2753$ radian day^{-1} (normalized by a_S/R_S in simulations). A factor of $1/\sqrt{\mu}$ has been absorbed into the definition of $\mathbf{B}$.

[14] Following *Feng et al.* [2010] and *Feng et al.* [2012], the energy-source term in the energy equation Q_e is given as follows:

$$Q_e = Q_1 \exp\left(-r/L_{Q_1}\right) + Q_2(r-1)\exp\left(-r/L_{Q_2}\right)$$

where r is the heliocentric distance, $Q_2 = Q_0 C_a'$ with $C_a' = C_a/\max(C_a)$ and $C_a = \frac{\left(5.8 - 1.6e^{\left[1-(\theta_b/8.5)^3\right]}\right)^{3.5}}{(1+f_S)^{2/7}}$. Here, Q_1 and Q_0 are given as $1. \times 10^{-9}$ Jm^{-3} s^{-1} and 1.5×10^{-7} Jm^{-3} s^{-1} respectively. L_{Q_1} and L_{Q_2} are set to be 1 and 0.8. This heating coefficient C_a is a function of two coronal parameters: flux tube expansion factor (f_S), and the minimum angular separation θ_b between an open field foot point and its nearest coronal hole boundary [*Arge et al.*, 2003; *Owens et al.*, 2005]. This consideration is motivated by the fact that solar wind speed is inversely related with the expansion factor f_S and that high speed wind from the center of a coronal hole has large θ_b and low speed wind from the hole boundary has a small θ_b.

[15] The calculation described here is performed by SIP-AMR-CESE MHD model, which has been described in detail by *Feng et al.* [2007, 2010] and *Feng et al.* [2012]. Here, only the basic features are given for completeness. To implement adaptive mesh refinement (AMR) of the SIP-CESE MHD model on the six-component grid system of the spherical shell domain, the governing MHD equations are transformed from the physical space (r, θ, ϕ) to the computational space (ξ, η, ζ) while retaining the form of conservation [*Jiang et al.*, 2010; *Feng et al.*, 2012], and the SIP-AMR-CESE MHD model is implemented in the reference coordinates by utilizing the parallel AMR package PARAMESH [*MacNeice et al.*, 2000; *Olson*, 2006].

[16] The computational region used in this paper extends from 1 to 27 R_s. Initially, the computational domain is divided into $8 \times 4 \times 4$ blocks with each block consisting of $6 \times 6 \times 6$ cells, and the blocks near the Sun are refined to have two refinement levels. To start the computation, the Parker's hydrodynamic isothermal solar wind solution [*Parker*, 1963] is used to give the initial values of the plasma density, ρ, gas pressure p, and the plasma velocity $\mathbf{u}$. At the same time, the potential magnetic field based on the daily-updated magnetic field synoptic data of the first day in Year 2007 is calculated in the corona as our initial magnetic field input. Here, the initial temperature and number density on the solar surface are prescribed to be 1.3×10^6 K and 1.5×10^8 cm^{-3}, respectively. Then, we integrate the MHD equations in time by relaxation until a converged steady-state equilibrium is achieved. In what follows, the solar wind solution is updated by being subjected to the time-dependent solar surface boundary conditions (described in next section) driven by daily-updated magnetic field synoptic data to obtain the coronal responses to the surface magnetic field variations in Year 2007. During the calculation, Δr is not uniform, which can be referred to *Feng et al.* [2012]. In practice, with the use of 96 MPI processes it takes about 45 hours' wall time (about 4320 CPU hours) with cores at 2.4 GHz to run MHD-DUSM model for a full CR, which is about fifteen times longer than that to run the MHD-MSM simulation for CR 2061.

3. Treatments of Solar Surface Boundary

[17] In this paper, we explore the coronal evolution by investigating the coronal responses to the changing magnetic field measured on the solar surface instead of computing a time-sequence of successive steady-state coronal solutions based on a set of magnetograms from WSO. To do this, we input a sequence of daily-updated magnetic field synoptic charts, in which the magnetic fields change at a rate corresponding to real time. Since the cadence of the daily-updated synoptic maps is about 24 hours, the magnetic field data on the solar surface are prepared by simply taking the difference of the two time sequences of the maps and then linearly increasing with time to drive the evolution. The expression used to update the radical magnetic field B_r on the solar surface for next time step is given as

$$B_r(\theta,\phi)^{n+1} = B_r(\theta,\phi)^n + \Delta B_r(\theta,\phi)\Delta t \tag{4}$$

with

$$\Delta B_r(\theta,\phi) = \frac{(B_r(\theta,\phi))_{m+1} - (B_r(\theta,\phi))_m}{24 \times 3600} \tag{5}$$

where Δt is the usual time step restricted by the Courant-Friedrichs-Lewy (CFL) condition, m denotes the mth daily-updated synoptic map and n is the nth time step.

[18] Just as *Yeh and Dryer* [1985] pointed out, the constraint, $\nabla \times \mathbf{E}_t = -\frac{\partial \mathbf{B}_r}{\partial t}$, should be satisfied on the boundary surface so that the sinusoidal condition, $\nabla \cdot \mathbf{E} = 0$, will be preserved. That is to say, when we keep B_r on the solar surface fixed in time, the tangential component of the electric field at the boundary, $\mathbf{E}_t$, is generally set to zero. However, when B_r varies with time, it is necessary to specify a non-zero $\mathbf{E}_t$ to make the flux evolution match the observed changes of the magnetic field [*Mikić et al.*, 1999] on the boundary surface. Furthermore, the monopolar component in each magnetogram is subtracted out as *Linker et al.* [1999] did before being used in the computation. According to the generalized Helmholtz theorem in the classical electromagnetic theory [*Song et al.*, 1999], the $\mathbf{E}_t$ can be separated into two parts: one is an irrotational component expressed by the gradient of a scalar function and the other part is a solenoidal field denoted by the rotation of a radial vector function: $\mathbf{E}_t = \nabla_t \Phi + \nabla_t \times (\Psi \hat{e}_r)$, where Φ and Ψ are arbitrary functions of θ and ϕ, and ∇_t indicates tangential derivative operator in the $\theta - \phi$ plane. Obviously, the first term represents the effects of the transverse magnetic field (i.e., the shear and the normal electric current), whereas the second term varies with the magnetic flux of B_r. Therefore, we only use a nonzero Ψ to describe the tangential electric field on the solar surface because the line-of-sight magnetograms can only provide the radial component of the magnetic field. Combining Faraday's law of electromagnetic induction $\nabla \times \mathbf{E}_t = -\frac{\partial \mathbf{B}_r}{\partial t}$ with $\mathbf{E}_t = \nabla_t \times (\Psi \hat{e}_r)$, we can get

$$\nabla_t^2 \Psi = \frac{\partial \mathbf{B_r}}{\partial t} \tag{6}$$

Once we get $\frac{\partial \mathbf{B_r}}{\partial t}$ from equation (5), we can solve equation (6) on the solar surface to obtain the potential Ψ, thus specifying the evolution of $\mathbf{E}_t$. From the ideal MHD condition

$$\mathbf{E}_t = -(\mathbf{u} \times \mathbf{B})_t \tag{7}$$

we can obtain two additional constraints of the bottom boundary conditions on the solar surface. For another five bottom boundary conditions to specify the evolution of the remaining seven physical quantities (i.e., ρ, p, v_r, v_θ, v_ϕ, B_θ, B_ϕ), please refer to Appendix A.

[19] It should be mentioned that equation (6) is solved on the solar surface by a direct fast Poisson solver [*Lai and Wang*, 2002], and the daily-updated magnetic field synoptic charts are preprocessed before being input into the calculation. Due to the line saturation effects, a saturation factor of 1.8 is chosen to modify the observed magnetic field strength of magnetograms according to the calibration analysis of WSO and other solar observatories [*Svalgaard et al.*, 1978; *Hu et al.*, 2008]. To remove the projection effects, B_r is specified at the solar surface with the relationship $B_r = B_{\rm los}/\cos\theta$, where θ is the heliographic latitude and $B_{\rm los}$ is the measured line-of-sight photospheric field, by supposing that the magnetic field is radial at the photosphere [*Wang and Sheeley*, 1992; *Luhmann et al.*, 2002]. At the same time, the polar magnetic fields are completed by the expression $B_r = B_p \cos^8\theta$, where B_p is the field strength at the very pole [*Svalgaard et al.*, 1978; *Wang and Sheeley*, 1988]. Finally, the monopolar component in the data is subtracted out as *Linker et al.* [1999] did.

4. Numerical Results

[20] This section presents the evolution of the large-scale coronal structures during Year 2007 obtained from the MHD-DUSM simulation. To validate the simulated results, we compare them with the available coronal and interplanetary observations. In sections 4.1, 4.2 and 4.3, the changing features of the coronal structures obtained by the 3D MHD-DUSM model will be compared with the observations from the Extreme Ultraviolet Imagers (EUVI) and the white-light measurements from the inner coronagraph (COR1). Both EUVI and COR1 are parts of the Sun Earth Connection Coronal and Heliospheric Investigation (SECCHI) [*Howard et al.*, 2008] instrument suite on board the spacecraft of the Solar Terrestrial Relations Observatory ahead of the Earth (STEREO A). In addition, the polarized brightness (pB) observations from the Large Angle Solar COronagraph (LASCO) C2 onboard the Solar and Heliospheric Observatory (SOHO) are also used to check the MHD-DUSM model. In section 4.4, a detailed comparison will be performed between the simulated results and the interplanetary measurements from both Ulysses and OMNI, which are mapped to 20 R_S from the interplanetary space, as done by *Neugebauer et al.* [1998] and *Linker et al.* [1999]. In section 4.5, we will display some results from the MHD-MSM for CR 2061 with the same code in order to demonstrate the differences between these two MHD models. It should be noted that, for clarity, we only present the simulated results of 4 CRs in this section, and the remaining results are arranged in Appendix B.

4.1. Comparison With Disc Images

[21] Coronal holes are believed to be associated with open magnetic field regions and to be the source regions of fast solar wind [*de Toma*, 2011], in which, due to the expansion of the solar wind, the plasma has lower density and temperature than in other coronal regions, such as the streamers. Thus, coronal holes are typically identified as dark regions in ultraviolet (UV) and X-rays radiations by their low emission intensity [*Linker et al.*, 1999]. Here we assume that the observed coronal holes correspond to the open-field regions. In order to determine the boundaries between the open-field and closed-field regions for both the MHD-DUSM and PFSS results, we trace the 3D magnetic field lines to distinguish the regions of open field on the solar surface, from which the field lines reach the outer boundaries at 5 R_S for the MHD-DUSM model and at 2.5 R_S for the PFSS model [*Feng et al.*, 2010].

[22] Figure 1 displays the synoptic maps of coronal holes at 1 R_S from the SECCHI EUVI observations (Column 1), MHD-DUSM model (Column 2) and PFSS model (Column 3) for CRs 2052, 2055, 2058 and 2061. The synoptic images of EUVI observations are constructed by assembling the daily-observed disk images. In Columns 2 and 3, the modeled coronal holes (i.e., the open-field regions) are represented with black regions and the other regions (i.e., the closed-field regions) with white regions. It should be noted that for the purpose of comparison with the observations and PFSS results, we select the MHD-DUSM result on the last day of each Carrington rotation (CR), in which the radial magnetic fields on the solar surface have been updated completely by the daily observed magnetograms.

[23] Seen from both the observations and the simulations in Figure 1, the most pronounced coronal feature during the whole year is the presence and persistence of the mid- and low-latitude coronal holes (MLCHs), which occupy a significant portion of the solar surface. In fact, *Abramenko et al.* [2010] found that there were several isolated long-lived equatorial coronal holes dispersed on the solar surface during 2007, which was different from the observations in the previous solar minima. Now we examine the isolated low-latitude MLCH centered at about $\theta = -10^\circ$ and $\phi = 25^\circ$. The EUVI images show that the MLCH first appears in CR 2052 (although rather weak in the observation) and survives until CR 2058 for nearly 6 rotations. However, in both the MHD-DUSM and PFSS results, the life of the MLCH is shorter than the observation by about a CR, and its location is too far north. In addition, its size is too large in the MHD-DUSM simulation as compared to that in the EUVI image. These discrepancies are possibly attributed to the inaccurate polar fields caused by the imperfect interpolation of data gaps in the polar regions. In fact, some studies have revealed that polar fields have significant effects on the distributions and sizes of the coronal holes [*Wang et al.*, 2009]. Another long-duration isolated MLCH from Columns 1 and 2 is located at $\theta = 0^\circ$ and $\phi = 220^\circ$–240°, firstly detected in CR 2057, and continuously observed throughout the end of this year. *Abramenko et al.* [2010] analyzed this persistent MLCH in detail, and found that it survived almost two years, began to shrink gradually during 2009 May, and finally vanished in June.

[24] As for the polar coronal holes (PCHs), we can see that both the EUVI observations and the MHD-DUSM model results reveal that they continuously change during the year of 2007 and appear different in shapes and sizes from one rotation to another. Basically speaking, the southern PCH is mainly characterized by two extended CHs and more evident than the northern one. The extended CH at about $\phi = 120^\circ$ in CR 2059 appears at the start of the year 2007, then increases

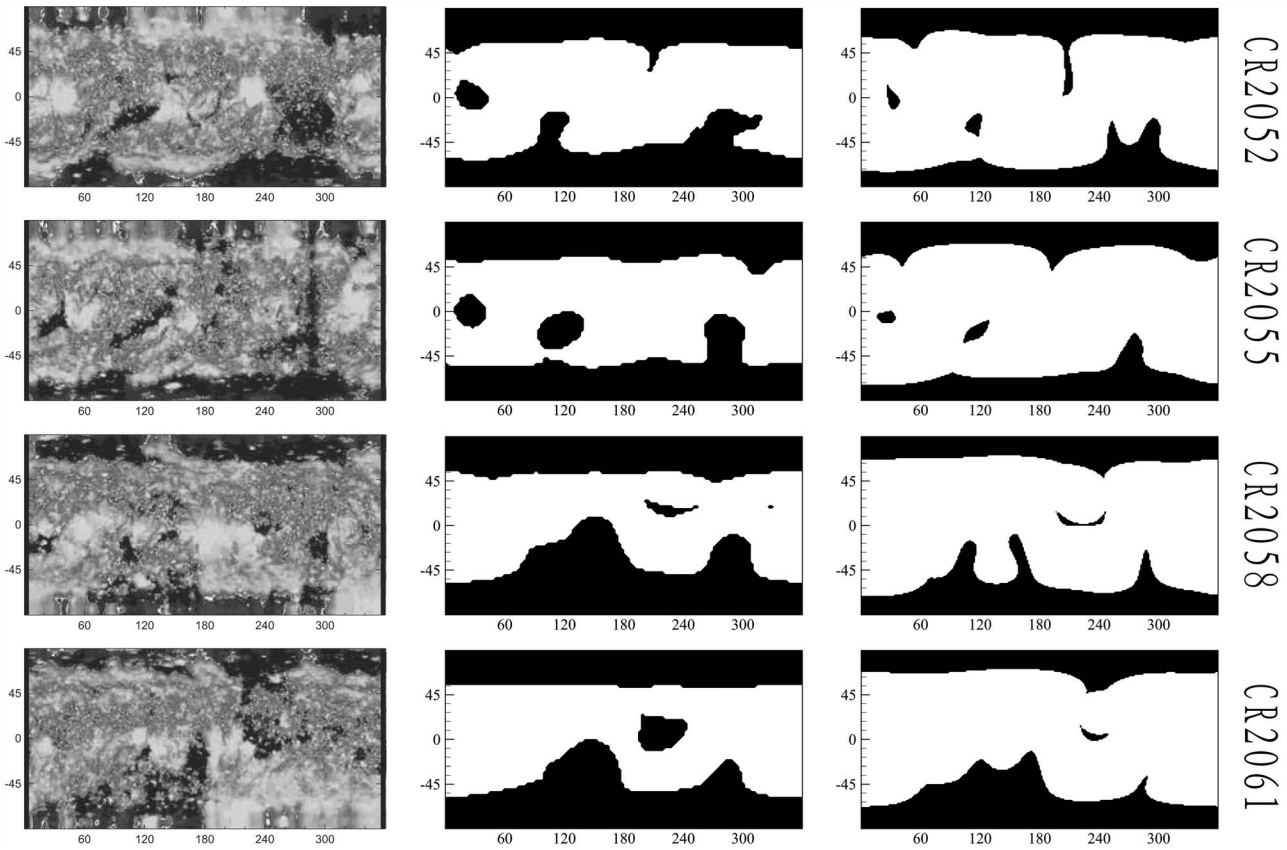

Figure 1. Synoptic maps of the coronal holes at 1 R_S for CRs 2052, 2055, 2058 and 2061. The first column is the observation by STEREO-A SECCHI EUVI 195 Å. The second and third columns are the simulated coronal holes from the MHD-DUSM and PFSS models, respectively.

rapidly and remains a relatively large size until the end of this year. However, the other extended CH about $\phi = 240°$ behaves somewhat differently seen from the observations and the MHD-DUSM simulations. The EUVI observations show that it is very big at the first sight, then decreases, and disappears completely in CR 2064, whereas it extends more northward in the MHD-DUSM model results, especially in CR 2058. Sometimes, the PCHs are a little patchy and are obscured by bright features, which have not been reproduced by both the MHD-DUSM and PFSS models.

[25] Comparing the modeled results with the observations, we can see that the MHD-DUSM has basically captured the features and evolution of the coronal holes. The shapes and distributions of the modeled open-field regions roughly agree with those of the observed CHs. However, there are some points worth noting. i) The areas of both PCHs in the EUVI image are smaller than those in the MHD-DUSM results, but larger than those in the PFSS model; ii) The shapes and sizes of extended PCHs are different among the EUVI observations, the PFSS and the MHD-DUSM results, and the MHD-DUSM results have much more extended PCHs than those from the PFSS model; iii) More isolated MLCHs can be clearly seen in the EUVI measurements, although the MHD-DUSM model obviously captures the two largest and most stable isolated ones with one centered at about $\theta = -10°$ and $\phi = 30°$ and the other at $\phi = 25°$ and $\phi = 240°$. However, the isolated coronal holes in the PFSS model are much smaller than those from both the observations and MHD-DUSM calculations; iv) The evolution of both the extended PCHs and the isolated MLCHs in the observations is more significant than those revealed in the MHD-DUSM and PFSS models.

[26] It is also instructive to examine the distributions of the number density, temperature, and radial speed on the solar surface with time-dependent inner boundary conditions described in section 3. Figure 2 shows the synoptic maps of the simulated number density N (unit: 10^8 cm^{-3}), temperature T (unit: 10^6 K), and radial speed v_r (unit: km s^{-1}) at 1 R_S for CRs 2052, 2055, 2058 and 2061, where the black lines denote the magnetic neutral lines. As expected, with the time-dependent inner boundary condition, N, T and v_r vary reasonably on the solar surface with respect to the magnetic field topology obtained by the MHD-DUSM model. In the open-field regions, i.e., the coronal holes as shown Figure 1, the plasma achieves higher speed, lower temperature and density. However, the nearly stagnant plasma in the closed field regions is of higher temperature and density. The typical density at the base of the coronal hole obtained from the MHD-DUSM model is about 1×10^8 cm^{-3}, the temperature is 2×10^6 K and the radial speed is 5 km s^{-1}. Near the magnetic neutral lines, they are 2×10^8 cm^{-3}, 2.5×10^6 K and 0.5 km s^{-1}, respectively. Thus the typical ratios of the simulated parameters in the coronal hole to those in the streamer are about 1:2 for the proton number density, 1:1.3

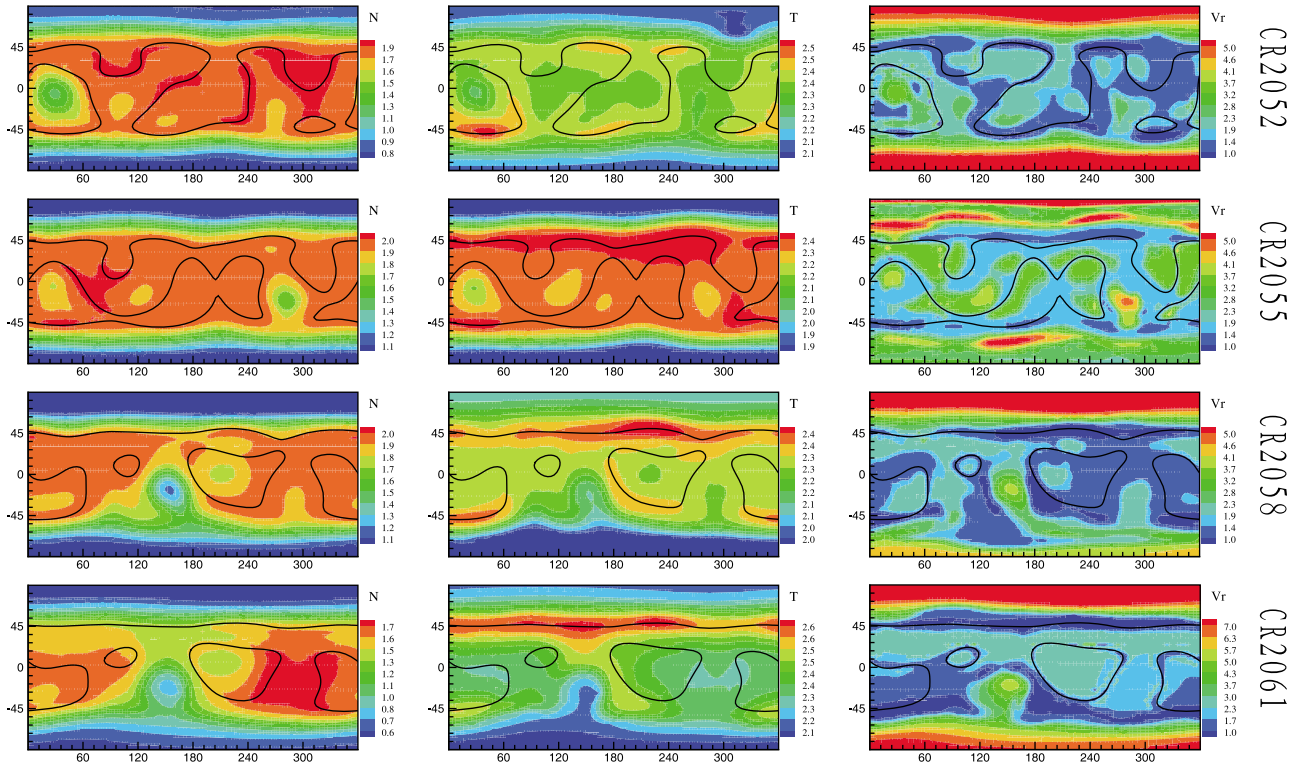

Figure 2. Synoptic maps of the simulated number density N (unit: 10^8 cm^{-3}), temperature T (unit: 10^6 K), and radial speed v_r (unit: km s^{-1}) at 1 R_S for CRs 2052, 2055, 2058 and 2061, where the black lines denote the magnetic neutral lines.

for the temperature and 10:1 for the radial speed. These numerical values of temperature and density are in good agreement with those derived from the analysis of the reconstructed STEREO/EUVI local differential emission measure (LDEM) for different coronal features [e.g., *Frazin et al.*, 2009; *Vásquez et al.*, 2010]. It should be also noted that from CR 2052 to 2064, the distributions of thin, cool and fast plasma are automatically adjusted to keep pace with the shapes and distributions of coronal holes, and the properties of the plasma density and radial velocity from the simulation are more sensitive to the associated magnetic field geometry than those of the temperature. Therefore, the model has indeed generated reasonable distributions of the plasma density, temperature and velocity on the solar surface due to the proper inner boundary treatments of combining the projected normal characteristic method and the mass flux limit with the evolution of radial magnetic field and the tangential component of the electric field.

4.2. Comparison With Synoptic pB Images

[27] The synoptic pB images obtained by a coronagraph are predominantly produced by the line-of-sight integrated electron density of coronal structures with the photosphere occulted. Thus, the bright regions shown in white light images are usually interpreted as the dense streamers viewed on the limbs and the dark regions as the less dense coronal holes. As the physical characteristics of the solar corona are generally thought to be controlled by coronal magnetic field, white-light images also reflect the coronal magnetic field configurations. It is believed that the observed white-light bright structures observed farther than 2.5 R_S are coincident in locations of the current sheets and therefore are closely related to the surfaces where the radial magnetic field Br changes its sign [e.g., *Wang et al.*, 1997; *Hu et al.*, 2008]. In this section, we will use the synoptic pB maps from the white-light observations of SOHO LASCO C2 and STEREO-A SECCHI COR1 to diagnose the 3D structures of the corona and to verify our MHD-DUSM results.

[28] Figure 3 presents the synoptic maps at 2.5 R_S for CRs 2052, 2055, 2058 and 2061. The first and second columns are the observed images at the east limb from SOHO LASCO C2 and at the west limb from STEREO-A SECCHI COR1. The synoptic images are constructed by extracting a slice of east or west limb data centered at r = 2.5 R_S from each of a 27.3-day successive LASCO C2 or SECCHI COR1 images, and arranging the strips in time-reversed sequences, where the vertical streaks represent coronal mass ejections [*Wang et al.*, 2002]. The third column is the simulated number density N (unit: 10^5 cm^{-3}). In the first, second, and third columns, the black solid lines denote the magnetic neutral lines from the MHD-DUSM model and the white lines from the PFSS model. The fourth column overlays the isolines of the radial magnetic field (unit: Gauss) on the contour maps of the simulated radial speed v_r (unit: km s^{-1}).

[29] From Figure 3, we can see that the current sheets of the four CRs calculated from both the MHD-DUSM and PFSS models are surrounded by the bright white-light structures at the east and west limbs. Most of the brightest structures lie where the latitudes of the current sheet vary least with longitude. *Wang et al.* [2000] pointed out that at

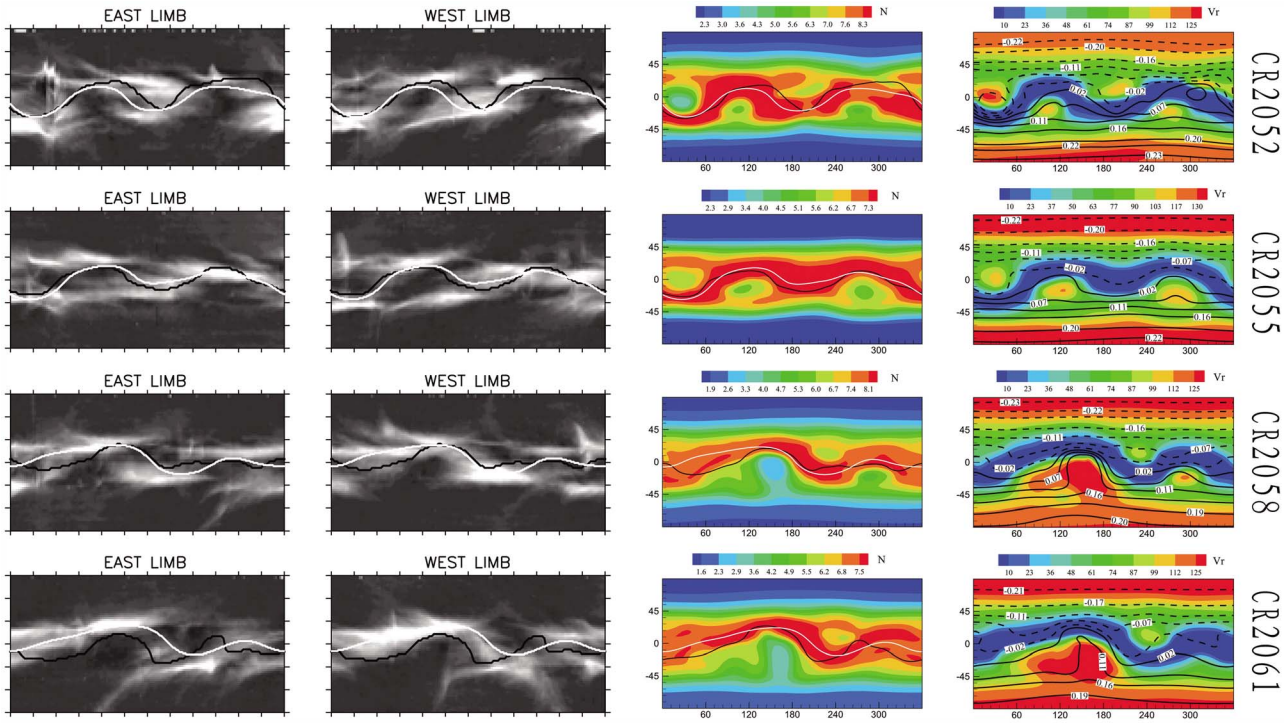

Figure 3. Synoptic maps at 2.5 R_S for CRs 2052, 2055, 2058 and 2061. The first and second columns are the white-light pB observations at the east and west limbs from SOHO LASCO C2. The third column is the simulated number density N (unit: 10^5 cm $^{-3}$). In the first, second, and third columns, the black lines denote the magnetic neutral lines from the MHD-DUSM model and the white lines from the PFSS model. The fourth column overlays the isolines of the radial magnetic field (unit: Gauss) on the contour maps of the simulated radial speed v_r (unit: km s^{-1}).

these locations, the plasma sheet was oriented edge-on in the sky plane and the number of electrons in the line of sight reached its maximum. For each rotation, a pronounced 4-sector structure of the current sheet, i.e., a rough double sinusoid, is located between the latitudes of $\pm 30°$ both in the observation and in the simulation at 2.5 R_S, which indicates that there is a strong quadrupole component originating in the observed photospheric field. Although the latitudes of the HCS along Carrington longitude range between 1° and 15°, the 4-sector structure is relatively stable throughout the whole year. During the evolution from CR 2052 to 2055, the current sheet reaches its maximum southward excursions at about Longitudes 60° and 200°, near which the current sheet bends sharply northward. From CR 2056 to 2060, the first maximum southward excursion of the current sheet at ϕ = 60° becomes flat gradually, and eventually disappears from CR 2061 to 2064. Whereas, the second maximum southward excursion at ϕ = 200° progressively increases in longitude and arrives at ϕ = 220° in CR 2064. The HCSs obtained from both MHD-DUSM and PFSS models have almost the same overall shape and location for each CR, and evolve in a similar manner during the year of 2007. However, there are also several local discrepancies between them. The HCSs from the MHD-DUSM model are more distorted and deflect more abruptly, compared with those from the PFSS model. In addition, the HCSs from the MHD-DUSM results displace a little southward relatively to those from the PFSS results. However, the bright structures in the white-light pB observations are more complicated than HCSs. Some very bright structures from observations and the high-density from the MHD-DUSM model are indeed far away from HCSs. The first region lies at 30°N in the first and last 30 degrees of longitudes during CRs 2052, 2055, and 2061. The other one is located at 30°S around Longitude 170° during CRs 2052 and 2055. It should be noted that the high-density regions from the MHD-DUSM model can also match some bright structures in the pB images other than those associated with the HCS. These high-density regions possibly result from the pseudo-streamers [*Wang et al.*, 2007; *Riley and Luhmann*, 2012], i.e., unipolar dense regions far from the neutral lines. More detailed analysis is beyond the scope of this paper and will be left for our future work.

[30] In Figure 3, we also present the distributions of the simulated proton number density, radial speed and radial magnetic field on the surface at 2.5 R_S. By examining these results, we can recognize that in each rotation, the locations of the bright structures in the white-light pB images at the east and west limbs, which are identified as the streamer belts, are characterized by the lowest velocity and highest plasma density in the simulation, and the dark regions are coincident with the locations of the increased flow speed and decreased plasma density. The high-density low-speed flow spans 20 degrees in latitude around the magnetic neutral line, whereas the low-density high-speed (LDHS) flow mainly covers the middle and high latitudes, where the magnetic field changes slowly. Meanwhile, the LDHS flow also scatters in a few low-latitude regions, which are associated with the isolated coronal holes or the persistent

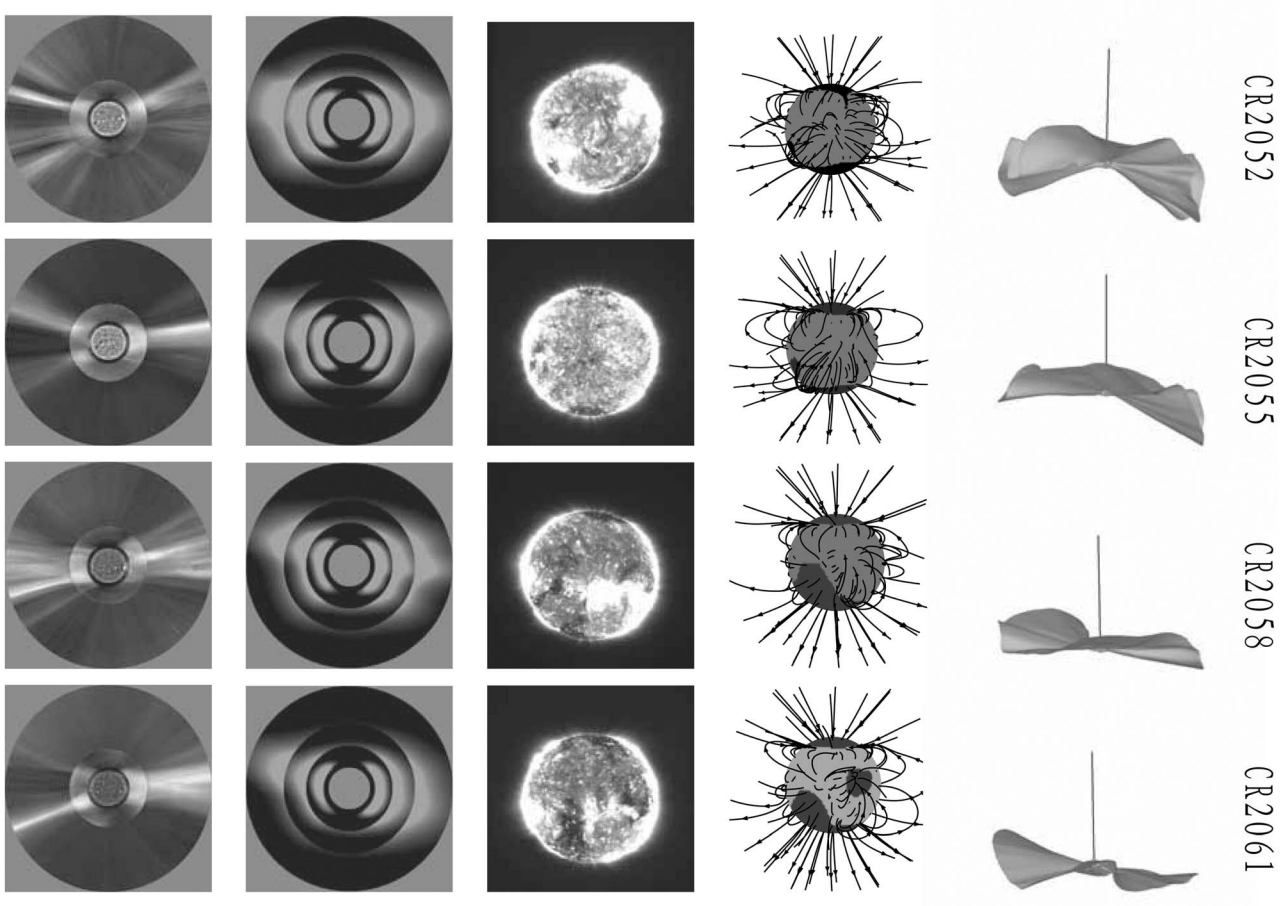

Figure 4. The coronal observations and simulated results on the meridional plane at ϕ = 90°–270° for CRs 2052, 2055, 2058 and 2061. Columns 1 and 2 are the pB images obtained by the coronal composite observations and the MHD-DUSM results from 1.15 to 6 R_S, respectively. Column 3 is the STEREO-A SECCHI EUVI 195 Å observation on the solar disk for the same days as in Column 1, and column 4 is the simulated 3D magnetic field lines from 1 to 2 R_S with open-field regions shown in black and closed-field regions in gray. The last column is the 3-D representations of the HCSs.

isolated MLCHs by combining Figure 3 with Figures 1 and 2. These LDHS flows produce the dark regions near the solar equator in white-light images at the east and west limbs. It can be also found that the differences in shapes and areas of the coronal holes on the solar surface between different rotations are also reflected on the distributions of the number density, radial speed and radial magnetic field on the surface at 2.5 R_S, which demonstrates that the time-dependent solar surface boundary condition can drive both the evolution of coronal holes and the corresponding evolution of streamer belts beyond 2.5 R_S. Besides, we can see that the typical values of the simulated number density and radial speed are about 7.5×10^5 cm^{-3} and 25 km s^{-1} near the current sheet and about 2.0×10^5 cm^{-3} and 110 km s^{-3} at middle and high latitudes, which are in good agreement with the results on the surface at 2.5 R_S near the solar minimum period from the empirical model developed by *Wei et al.* [2003]. Due to the presence of the coronal heating, the MHD-DUSM model basically yields the observed large contrasts in the number density and radial speed between open and closed field regions.

4.3. Comparison With Daily Observations

[31] To further demonstrate that the MHD-DUSM solution can describe the specific coronal observations, we present the results corresponding to some daily measurements. Figure 4 shows the evolution of the observed and simulated streamers and coronal holes during the year 2007 at about 27-day intervals between January 22 and December 15, which are correspondent to Day 13 of the associated CRs. The first column is the composite coronal pB image from 1.15 to 6 R_S, where the data from 1.15 to 2.3 R_S comes from Mauna Loa Solar Observatory (MLSO) Mark-IV coronameter observation, and the outer fields of view from 2.3 to 6 R_S are from LASCO C2 observations. The second column displays the derived pB images from the simulation results on the same plane shown in the first column, in which the images are enhanced inside 2.3 R_S, from 2.3 to 4 R_S and outside 4 R_S, separately. The third column is the disk observations from STEREO-A SECCHI EUVI 195 Å for the same views as the coronal composite images in the first column, and the fifth column is the simulated 3D magnetic

field lines from 1 to 2 R_S with open-field regions on the solar surface shown in black and closed-field regions at 1 R_S shown as gray. The last column is the 3-D representation of the HCS.

[32] Figure 4 shows that in each pB image, the bright, thin streamers are restricted to a narrow range of lower latitudes and the higher latitudes are dominated by the large, dark polar coronal holes. Almost every observed images show very bright long streamer-like structures above 3 R_S at the east and west limbs, although they seem wider in the simulation results. These streamer-like structures result from the emission of the classic helmet streamers close to the sky plane. Both the simulation and the observations reveal that these streamer-like structures do not extend radially outward from their foot points, but cover relatively large latitudes near the Sun. However, except the brightest and sharpest structures at both limbs, there are also diffusive and less bright radial structures outside 3 R_S, some of which disappear in some CRs and then reappear in other CRs. Seen from the Mark-IV coronagraph observation and the simulated results presented in Figures 3 and 4, most of these diffusive structures result from the projection effects of the high-density structures off the plane of sky, which are associated with a single, warped current sheet encircling the Sun as shown in the last row of Figure 4. However, some of the diffusive structures may originate from the pseudo-streamers as discussed in section 4.2. Besides, in both the Mark-IV and the LASCO C2 observations, there were sharp polar boundaries between the brightest streamers and the adjacent coronal hole regions. By contrast, the equatorward boundaries, where the lines of sight pass the streamer materials out of the plane of the sky, are relatively diffusive in appearance as demonstrated by *Wang* [1996]. Although the coronal large-scale structure changes very slowly from one CR to another near the solar minimum, there are still some changing features of the streamers and coronal holes during this period. On the east limb, there are initially 2 streamer-like structures. They are almost at the equator on CR 2054 and then go back north and split in CR 2056. The bright long streamer-like structure on the west limb of each image is clearly moving south during the year, which first appears at about $\theta = 20^\circ$ in CR 2052, then drifts towards and crosses the solar equator, and finally reaches about $\theta = -30^\circ$ in CR 2064.

[33] As far as the coronal holes are concerned, the fourth column shows that there are only small-sized isolated MLCHs near the east disk from CR 2052 to 2056 and the simulation has produced some relatively larger ones. In CR 2057, the isolated MLCH first appears at the center of the disk, and persists till the end of this year although its shapes and sizes slightly change from one rotation to the next. Nevertheless, the extended southern coronal hole near the east limb behaves somewhat different, which first appears on the south hemisphere in CR 2058. Its size increases from CR 2059 to CR 2061, then decreases from CR 2062 on and becomes the largest in CR 2064. Comparisons of the simulated results with the observations evidently shows that the basic 3D structure of the streamer belt and coronal holes have been captured by the MHD-DUSM model. Their evolution shows a general consistency with the observations except that the extended southern coronal hole near the west limb obtained from the MHD-DUSM model appears about one CR later, which is possibly due to the longitudinal inaccuracy of the simulation during the coronal evolution.

4.4. Comparison With Interplanetary Measurements

[34] Since there are no in-situ solar wind observations near the outer boundary in our simulation for us to verify the simulated results, we map the interplanetary measurements back to 20 R_S by using a ballistic approximation, in which the variations in longitude are computed from the time interval required for a plasma parcel traveling from 20 R_S to the spacecraft location with the in-situ measured solar wind velocity. In order to test the simulated results at both high and low heliographic latitudes, we compare the MHD-DUSM model predictions with the mapped observations from both Ulysses and OMNI data. At the same time, the Wang-Sheeley-Arge (WSA) model [*McGregor et al.*, 2011a, 2011b] is also employed to check the MHD-DUSM model.

[35] Figure 5 displays the synoptic images at 20 R_S for CRs 2052, 2055, 2058 and 2061. In every CR, the left column is the simulated radial speed v_r (unit: km s^{-1}) from the MHD-DUSM model and the right column is the predicted radial speed from the WSA model. The 1-hour averaged Ulysses' observations are mapped back to 20 R_S, beyond which we assume that there is no changes for the radial speed. The mapped points are plotted versus heliographic latitude and Carrington longitude with the black-line bounded regions representing the distributions of the measured radial speed. In all these maps, the same contour levels for the radial speed are used as shown in the bottom. Figure 6 shows temporal profiles of the radial solar wind speed and the radial magnetic field polarities from the simulated results of the MHD-DUSM model (red dotted lines), the WSA model (blue dashed lines) and the mapped observational results from the OMNI data (black dashed lines) at 20 R_S for CRs 2052, 2055, 2058 and 2061.

[36] As shown in Figure 5, when Ulysses orbiting in the high latitudes (>50°) far away from the current sheet, both the MHD-DUSM simulation and the WSA model have well reproduced the observations of the solar wind speed, and the MHD-DUSM simulation has also predicted the presence of the intermediate speed solar wind at the middle latitudes during CR 2057 (see Appendix B). The MHD-DUSM model gives a relatively wider low speed solar wind than the modified WSA model. However, both models have overestimated the coverage of the high speed solar wind from the southern polar coronal hole from Longitudes 50° to 170° for CRs 2058 and 2059. The MHD-DUSM simulation has also underestimated the solar wind speed along Latitude 40°N between Longitudes 30° and 230° in CR 2061.

[37] *Tokumaru et al.* [2010] pointed out that the low-latitude regions during the 1996 and 1986 minima were dominated by low-speed solar wind. However, for Year 2007, both the modeled achievements and the mapped measurements near Earth observe a different picture with some intermediate or fast streams interspersing the low-speed streams. The phasing of the fast streams predicted by both the MHD-DUSM and WSA models is offset by less than two days from the observations. Meanwhile, the continual emergence of these equatorial fast wind leads to the significant increase of the averaged solar wind speed at the equator with the occurrence rate at about 600 km s^{-1} almost

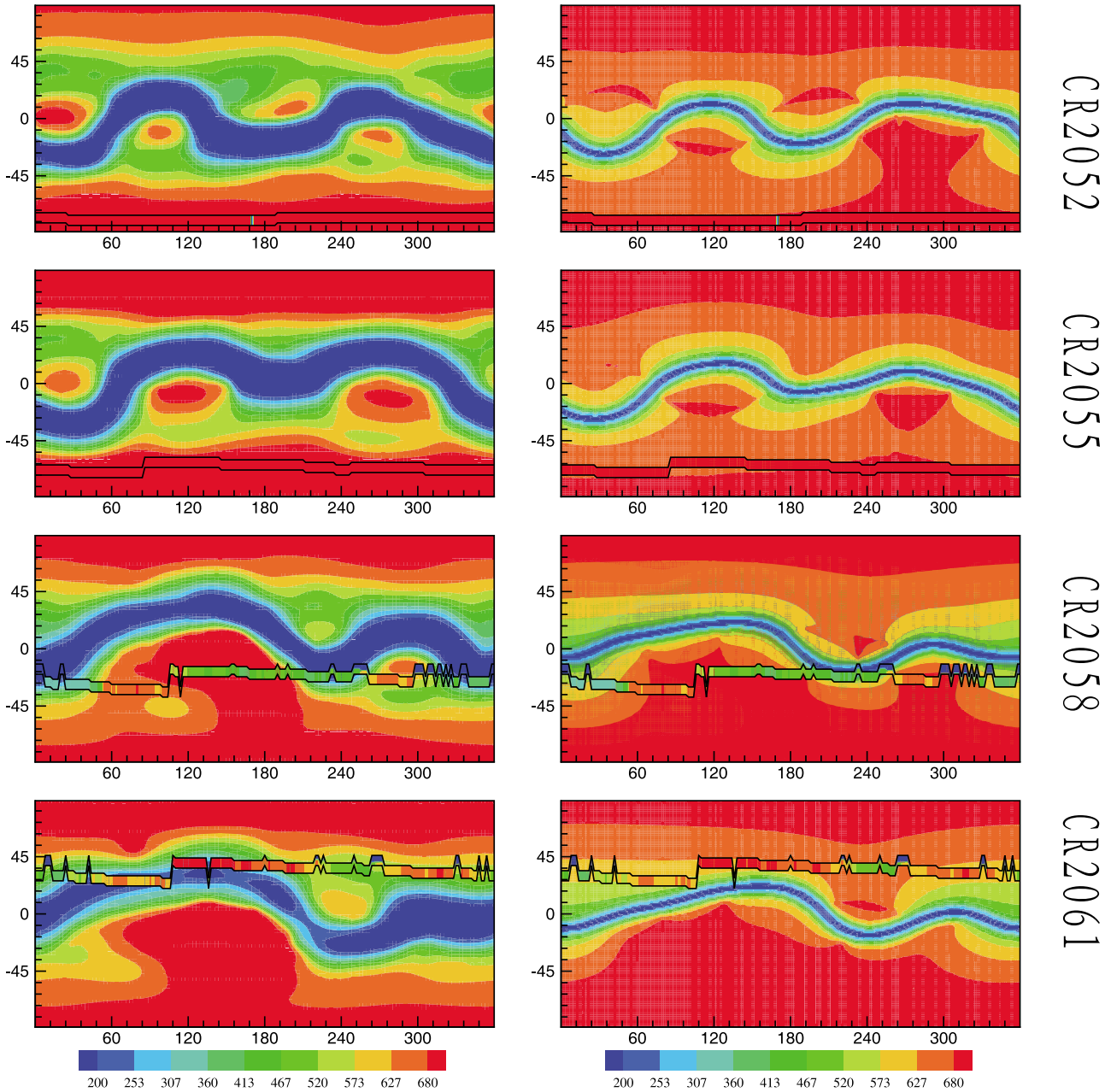

Figure 5. Synoptic images of the mapped Ulysses' measurements and models' results at 20 R_S for CRs 2052, 2055, 2058 and 2061. In every CR, the left column is the simulated radial speed v_r (unit: km s^{-1}) from the MHD-DUSM model and the right column is the predicted radial speed from the WSA model [*McGregor et al.*, 2011b]. The mapped points are plotted versus heliographic latitude and Carrington longitude at 20 R_S with the observations from Ulysses shown in black-line bounded regions. In all these maps, the same contour levels for the radial speed are used as shown in the bottom.

comparable to that at about 400 km s^{-1} or 700 km s^{-1} as pointed out by *Tokumaru et al.* [2010]. Another important point revealed by the MHD-DUSM model and the observations is that the solar wind speed structures evolve considerably during the year 2007. The two broad fast streams are first discerned in CRs 2052–2053, and the first fast stream becomes less prominent in CR 2054. In CR 2055, the two broad fast streams almost disappear. The fast stream at about $\phi = 30°$ becomes more evident since 2056, but it only lasts to the end of CR 2059. The area of the first broad fast stream at about $\phi = 130°$ is over estimated by both the MHD-DUSM and WSA models, which becomes evident after CR 2060. For the fast stream at about $\phi = 220°$, the MHD-DUSM model have basically reproduced its evolution during 2007.

[38] As far as the magnetic polarities in low latitudes are concerned, the MHD-DUSM model predicts them with a very satisfactory accuracy except for a few errors in CRs 2059, 2060 and 2061 due to the waves and perturbations occurring in the field, which leads the opposite polarity to be

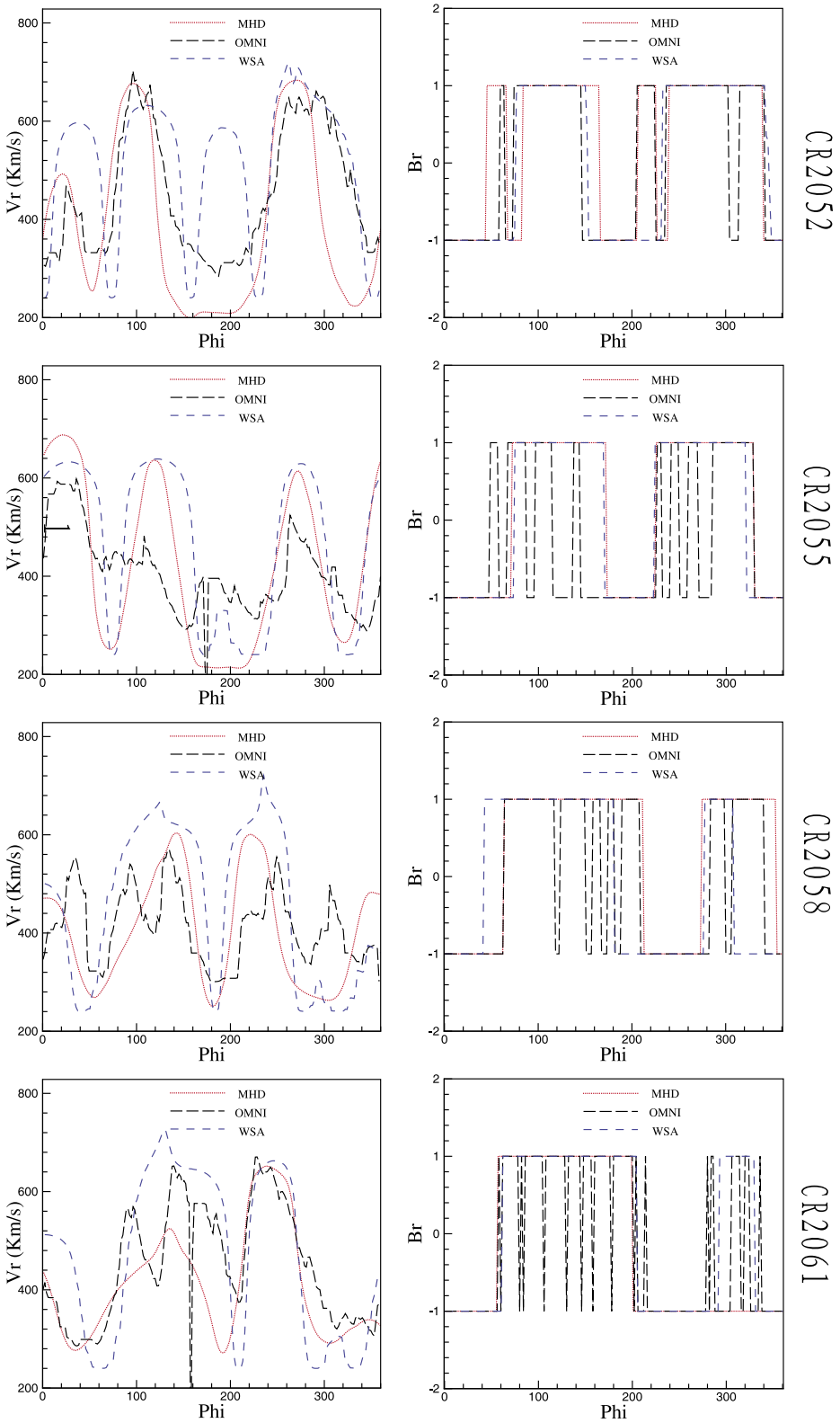

Figure 6. Comparisons between the mapped interplanetary measurements from OMNI data and the models' results for CRs 2052, 2055, 2058 and 2061. For each CR, the left column shows the temporal profiles of the radial speed v_r (unit: km s^{-1}) from the mapped observations (black dashed lines), the MHD-DUSM (red dotted lines), and the WSA formula (blue dashed lines). The right column presents the profiles of the radial magnetic field polarities obtained from the mapped observations (black dashed lines), the MHD-DUSM model (red solid lines), and the WSA formula (blue dashed lines), where "+1" stands for the radial magnetic field away from the Sun and "−1" towards the Sun.

Table 1. Statistical Analysis Between the Models' Results and the Mapped OMNI Data

	$C_{Vr-\mathrm{MHD}}$	$C_{Vr-\mathrm{WSA}}$	$R_{Br-\mathrm{MHD}}$	$R_{Br-\mathrm{WSA}}$
CR 2052	0.745	0.578	0.817	0.845
CR 2053	0.578	0.306	0.879	0.842
CR 2054	0.694	0.512	0.770	0.743
CR 2055	0.345	0.360	0.665	0.680
CR 2056	0.402	0.599	0.765	0.648
CR 2057	0.339	0.401	0.641	0.674
CR 2058	0.384	0.374	0.802	0.715
CR 2059	0.339	0.434	0.773	0.780
CR 2060	0.828	0.680	0.768	0.807
CR 2061	0.745	0.710	0.867	0.839
CR 2062	0.651	0.538	0.846	0.822
CR 2063	0.794	0.760	0.907	0.653
CR 2064	0.861	0.811	0.763	0.742

measured rather than the true field polarity [*Lepri et al.*, 2008]. Generally speaking, the sector structure of the magnetic field predicted by the MHD-DUSM model seems closer to the observation than that from the PFSS model. We can see that the number of different sectors predicted by the MHD-DUSM model approaches to that from the observations, despite that the crossing longitudes are not well aligned, with somewhat later or earlier than the modeled passage of the current sheet. Furthermore, the sector structures from the PFSS model are much more uniform than those from both the observation and the MHD-DUSM model.

[39] In order to quantitatively demonstrate the predicting ability of the MHD-DUSM model, we present the correlation coefficients between the radial speeds from the OMNI data and those from the MHD-DUSM ($C_{Vr-\mathrm{MHD}}$) and WSA ($C_{Vr-\mathrm{MHD}}$) models in Table 1. We also list the hit ratios of the simulated radial magnetic field polarities from these two models in this table, which are represented by $R_{Br-\mathrm{MHD}}$ and $R_{Br-\mathrm{WSA}}$. The table tells that both models give comparable and basically similar predicting results. There are 8 CRs whose correlation coefficients are greater than 50% for both models. They both give relatively poor predictions from CRs 2055 to 2059. For CRs 2055 and 2056, the relatively poor results are probably attributed to a series of small-scale transients intercepted by multi spacecraft near the Earth during this period [*Kilpua et al.*, 2009], which displaced the originally recurrent high-speed solar wind flow. The poor predictions for CRs 2057, 2058 and 2059 may result from the northward offset of the simulated low-speed solar wind band from the observations, which can be seen from Figure 5 and is possibly associated with our inaccurate interpolation of the polar fields. In addition, both models give much better prediction of the radial magnetic field polarities.

4.5. Comparison With the MHD-MSM Results

[40] To demonstrate the differences between the results from the MHD-DUSM and the MHD-MSM models, we will present the MHD-MSM results for CR 2061, which is chosen without any preference. Figure 7 displays the synoptic map of the simulated coronal holes at 1 R_S. Figure 8 is the synoptic maps of the simulated number density N and radial speed v_r, where the first row is N (unit: 10^8 cm^{-3}) (left column) and v_r (unit: km s^{-1}) (right column) at 1 R_S, and the second row is N (unit: 10^5 cm^{-3}) at 2.5 R_S (left column) and v_r (unit: km s^{-1}) at 20 R_S (right column), where the black-line bounded region denotes the mapped Ulysses' measurements. In Figure 8, the black lines denote the magnetic neutral lines. In Figure 9, we show a comparison for the simulated 3D magnetic field lines from 1 to 2 R_S between the MHD-DUSM (left column) and the MHD-MSM models (right column), where the contours represent B_r (unit: Gauss) on the solar surface. It should be mentioned that we select the same starting points at the photosphere to trace the field lines in order to make a direct comparison between these two MHD models.

[41] The most conspicuous difference between Figure 7 and Figure 1 is the behavior of the MLCH. The long-duration isolated MLCH centering at about $\theta = 0°$ and $\phi = 220°$ is very small and almost disappears in the MHD-MSM simulation. Meanwhile, the extension of CHs in the southern hemisphere is small, but the extended CH in the northern hemisphere is closer to the EUVI observation than that in the MHD-DUSM model. From Figure 8, we can see that the magnetic neutral line is relatively flat and the distributions of N and v_r on the solar surface are more regular and simpler than the results from the MHD-DUSM model. The densest regions at 2.5 R_S are highly concentrated near both sides of the the magnetic neutral lines. In addition, the radial speed in the CH can roughly be comparable to that from the MHD-DUSM model. Meanwhile, the distribution of the simulated radial speed v_r at 20 R_S in Figure 8 shows that the MHD-MSM overestimates the coverage of the high-speed solar wind from the southern polar coronal hole, and underestimates the coverage of the intermediate-speed solar wind at the middle latitudes. The high-speed solar wind observed by Ulysses during CR 2061 is also missed by the MHD-MSM simulation. As to the magnetic polarities at low latitudes, the MHD-MSM model predicts the less accurate crossing longitudes of the current sheet, but basically gives the four-sector structure for the passage of Earth.

[42] In Figure 9, we compared the magnetic field topologies obtained by both the MHD-DUSM and the MHD-MSM models. The adoption of daily-updated magnetograms has a significant effect on the organization of the magnetic field as compared to the MHD-MSM model. The most striking feature is that the MHD-DUSM model has captured the sheared field lines that are slightly aligned with the neutral line separating the different polarities. These sheared field lines indicates that the solar corona is far from the potential state, whereas the MHD-MSM is closer to a potential solution. In

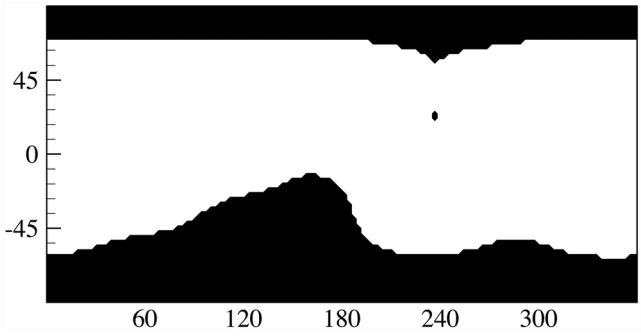

Figure 7. The synoptic map of the simulated coronal holes at 1 R_S from the MHD-MSM model for CR 2061.

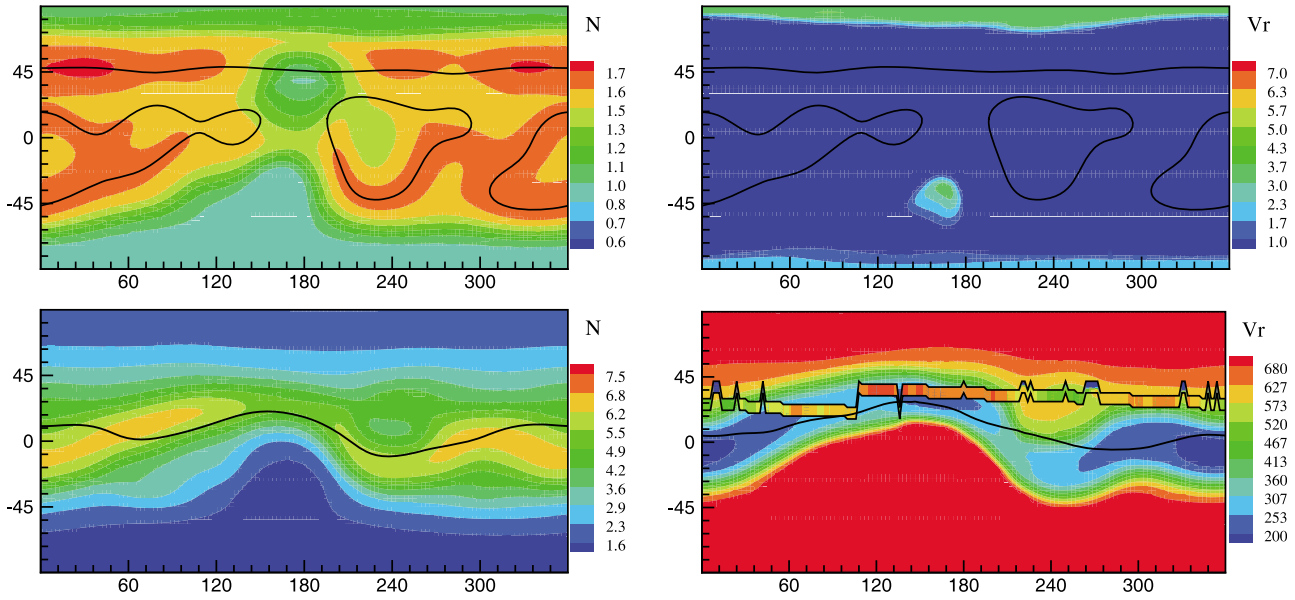

Figure 8. Synoptic maps of the simulated number density N and radial speed v_r from the MHD-MSM model for CR 2061. The first row is N (unit: 10^8 cm^{-3}) (left column) and v_r (unit: km s^{-1}) (right column) at 1 R_S. The second row is N (unit: 10^5 cm^{-3}) at 2.5 R_S (left column) and v_r (unit: km s^{-1}) at 20 R_S (right column), where the black-line bounded region denotes the mapped Ulysses' measurements. In all these maps, the black lines denote the magnetic neutral lines.

addition, the connection of both large and small closed loops is also different for these two MHD models. The MHD-DUSM model displays more small-scale loops at the base of corona, and it should be noted that these small-scale loops become deformed and appear nonpotential. Recently *Downs et al.* [2010] found that inclusion of the additional energy transport terms of coronal heating, electron heat conduction, and optically thin radiative cooling into the governing MHD

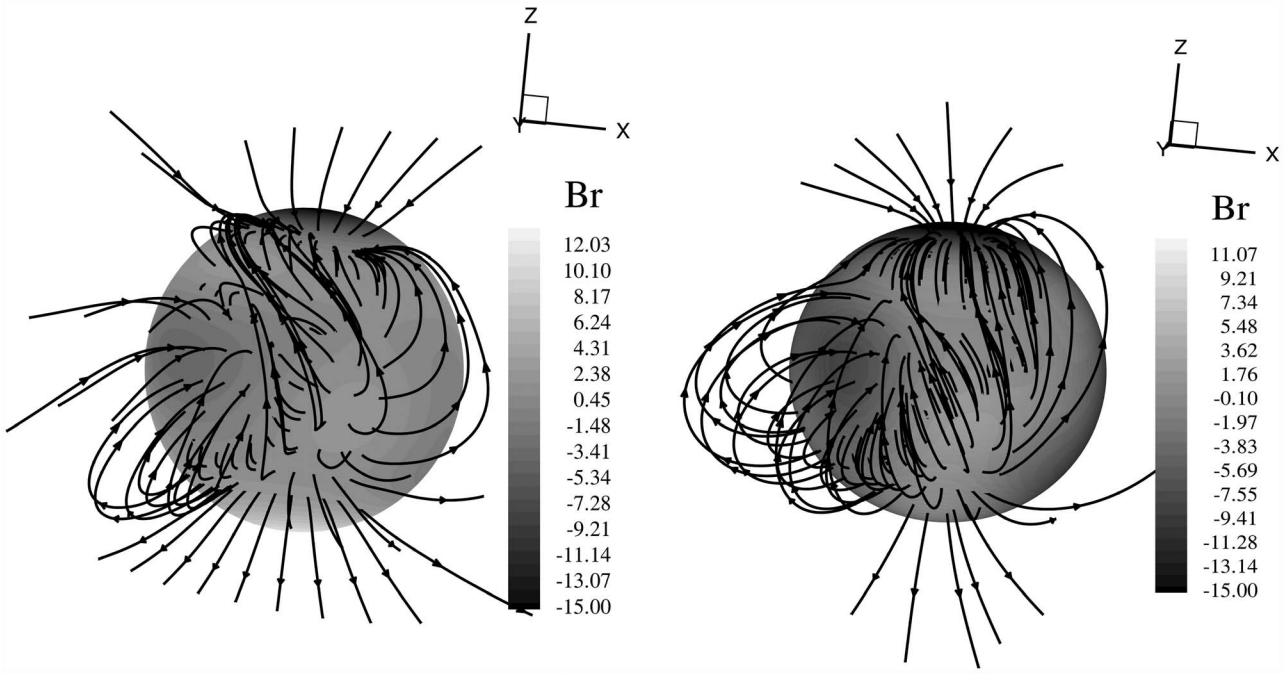

Figure 9. 3D representations of the simulated magnetic field from 1 to 2 R_S for CR 2061. The left figure is from the MHD-DUSM model, and the right figure from the MHD-MSM model, where the contours represent B_r (unit: Gauss) on the solar surface. The same starting points at the photosphere are used in tracing the field lines in order to make direct comparisons between these two MHD models.

energy equation enabled the evolution of the magnetic field during the simulation to be no longer strictly potential.

5. Summary and Discussion

[43] In this article, a newly developed 3D SIP-AMR-CESE MHD model [*Feng et al.*, 2012] is described and utilized to simulate the dynamic evolution of the global solar corona in 2007 driven by the daily-updated magnetic field synoptic data. In the model, we input a sequence of daily-updated magnetic field synoptic charts at a rate corresponding to real time to obtain the coronal responses of the changing magnetic field measured on the solar surface, instead of computing a time-sequence of successive steady-state coronal solutions based on each set of photospheric magnetogram as previous studies. The tangential component of the electric field at the bottom boundary is specified to make the magnetic field flux evolve to match the observed changes of magnetic field. To couple the observation and the 3D MHD model, the time-dependent solar surface boundary conditions derived from the method of projected characteristics are incorporated into the model. Under these boundary treatments, the bimodal solar wind is reproduced with slow, hot and dense wind in the closed field regions and fast, cooler and less dense wind in the open field regions. The typical ratios of the simulated plasma parameters in the coronal holes to those in the streamers can be comparable to the past investigations of in-situ interplanetary observations.

[44] The simulated results have been compared with the remote observations near the Sun and the mapped interplanetary measurements. The MHD-DUSM results are also checked by comparison with the results from both the standard PFSS model, and the newly improved WSA model, and the MHD-MSM model. Comparisons show that the MHD-DUSM model captures both the large persistent isolated MLCHs and the stable small PCHs. The shapes and distributions of the modeled coronal holes agree fairly well with those of the observed coronal holes. The MHD-DUSM model has also reproduced reasonably well the evolutions of the PCHs, the extended PCHs and the isolated MLCHs. Both the simulation and the observation display a stable pronounced 4-sector structure of the current sheet during 2007. The distributions of the simulated number density, radial speed and radial magnetic field on the surface at 2.5 R_S show that in each rotation, the locations of the bright structures in the white-light images of the east and west limbs are basically consistent with the regions of low velocity, high density and weak magnetic field in the simulation, and the dark regions with the areas of the high velocity, low density and strong magnetic field. In addition to producing the common coronal structures, the simulation can also describe specific coronal observations, such as the basic 3D structures and evolutions of the streamer belt and coronal holes during the selected simulation interval.

[45] Comparisons between the simulation results and the mapped interplanetary measurements from both Ulysses' observation and OMNI data demonstrate the MHD-DUSM model has recreated the unusual features of the solar wind in interplanetary space during this time period, such as the relatively low speed and the slightly dropping latitude width of the fast polar streams, and the persistent, pervasive and broad fast streams near Earth. The MHD-DUSM model has also identified the latitudinal changing trends of the solar wind speed, the transitions of the magnetic field polarities, and the significant evolution of the solar wind structure during this year. On the other hand, the MHD-DUSM model makes the corona much less potential as compared to the MHD-MSM model and the latter gives relatively flat HCS and can hardly reproduce the long-duration MLCH. It should be mentioned that although the MHD-DUSM is about 15 times slower than the MHD-MSM, it can be run much faster than real time (2 days for a CR) on a relatively small computing system (96 CPUs). In addition, quantitatively statistical analysis shows the MHD-DUSM model has a comparable predicting capability with the WSA model.

[46] Despite the fact that the MHD-DUSM model has partially succeeded in producing the observations, there are still many unsatisfactory points due to the factors discussed below. The first factor is the uncertainties in the photospheric magnetic field measurements including the data deficiency in the polar regions and unavailability of simultaneous magnetic field observations over the full solar surface. Therefore, we have to adopt various kinds of methods to complete the polar magnetic field [*Svalgaard et al.*, 1978; *Schrijver and De Rosa*, 2003; *Liu et al.*, 2007; *Sun et al.*, 2011], which is crucial to model the global large-scale coronal and interplanetary structures [*Arge and Pizzo*, 2000; *Luhmann et al.*, 2009]. Meanwhile, although the daily-updated magnetic field magnetograms are used, the data observed in the Earth-Sun direction at different instances have to be collected in order to make the chart covering all longitudes, which may miss the more accurate estimations of the coronal magnetic field and other parameters due to the coronal evolution. Other problems about the input magnetic field include the implementation of the polar field extrapolations to complete the magnetic field data, saturation corrections, and the unavoidable inconsistency in the generation of daily updated synoptic maps. The second factor is the coronal heating and solar wind acceleration used in the present paper, which assumes that coronal heating is approximately time-independent, at least on a large spatial scale. However, most coronal heating theories include time-dependent processes [e.g., *Klimchuk*, 2006; *Cranmer et al.*, 2007; *Cranmer*, 2010; *Tripathi et al.*, 2010; *van Ballegooijen et al.*, 2011]. At the same time, the presently used heating coefficients in the MHD model is calculated by the PFSS model with the daily-updated magnetic field synoptic charts, and thus lose their time-dependent characteristics since the simulated 3D magnetic field topology is in general different from the PFSS field structure. This imperfect assumption possibly causes the inaccuracy of the MHD results. The last point is that we should also include the tangential magnetic field to drive the MHD model if the high quality global vector magnetic field can be obtained, which may be expected from the SDO mission. Furthermore, to incorporate additional continuous observations for density, temperature and velocity will eventually lead to the more realistic data-driven, time-dependent solar wind model.

Appendix A: Treatment of Another Five Bottom Boundary Conditions

[47] Remembering that the evolution of B_r at the bottom boundary is given by equation (4), another five bottom

boundary conditions are needed to carefully specify the evolution of the remaining seven physical quantities (i.e., ρ, v_r, v_θ, v_ϕ, p, B_r, B_θ, B_ϕ), such that the incompatibility or inconsistentness in physics and mathematics can be avoided. The projected characteristic method, originated by *Nakagawa* [1980, 1981a, 1981b] and *Nakagawa et al.* [1987] and practically used by *Wang et al.* [1982]; *Wu and Wang* [1987]; *Wu et al.* [2001, 2006], *Wang et al.* [2011], *Hayashi* [2005]; *Hayashi et al.* [2006], and *Feng et al.* [2010], can minimize the physical inconsistency and reduce the unphysical vibrations near the sub-Alfvénic solar surface boundary to an acceptable level.

[48] In order to use the projected characteristics method along the radial direction (the normal of the inner boundary surface), the governing MHD equations (equation (3)) are cast in vector–matrix form under spherical coordinates [*Wu et al.*, 2001, 2006; *Hayashi*, 2005; *Wang et al.*, 2011]

$$\frac{\partial \mathbf{W}}{\partial t} = -\mathbf{A}\frac{\partial \mathbf{W}}{\partial r} - \mathbf{B}\frac{\partial \mathbf{W}}{r\partial\theta} - \mathbf{C}\frac{\partial \mathbf{W}}{r\sin\theta\partial\phi} + \mathbf{S} \equiv -\mathbf{A}\frac{\partial \mathbf{W}}{\partial r} + \mathbf{S_r} \quad \text{(A1)}$$

where $\mathbf{W}$ consists of the primary physical quantities such as $\mathbf{W} = (\rho, v_r, v_\theta, v_\phi, B_r, B_\theta, B_\phi)$. The detailed coefficient matrices $\mathbf{A}$, $\mathbf{B}$, $\mathbf{C}$ and source term $\mathbf{S}$ can be found in *Wu et al.* [2006], and will not be repeated. The Jacobian matrix $\mathbf{A}$ can be expressed as $\mathbf{A} = \mathbf{R\Lambda L}$, where $\mathbf{R}$ and $\mathbf{L}$ are the matrix form of the normalized right and left eigenvectors of $\mathbf{A}$, respectively, which satisfy $\mathbf{RL} = \mathbf{LR} = \mathbf{I}$ and $\mathbf{\Lambda}$ is the diagonal matrix whose diagonal elements are the eigenvalues. For the right and left eigenvectors, please refer to *Wu et al.* [2001, 2006] and *Hayashi* [2005]. Here, only the eigenvalues are given in a nondecreasing order,

$$\lambda_1 = v_r - v_f, \lambda_2 = v_r - v_A, \lambda_3 = v_r - v_s, \lambda_4 = v_r,$$
$$\lambda_5 = v_r, \lambda_6 = v_r + v_f, \lambda_7 = v_r + v_A, \lambda_8 = v_r + v_s,$$

where v_A is the Alfvén wave speed defined by $v_A = |B_r|/\sqrt{\rho}$, and $v_{f,s}$ are the fast/slow magneto-acoustic speeds given by

$$v_{f,s} = \sqrt{\frac{1}{2}\left(\frac{\gamma\, p + \mathbf{B}\cdot\mathbf{B}}{\rho} \pm \sqrt{\left(\frac{\gamma\, p + \mathbf{B}\cdot\mathbf{B}}{\rho}\right)^2 - 4\frac{\gamma\, p\, B_r^2}{\rho^2}}\right)}.$$

By multiplying the matrix $\mathbf{L}$ from the left, equation (A1) becomes

$$\mathbf{L}\frac{\partial \mathbf{W}}{\partial t} = -\mathbf{L}\left(\mathbf{R\Lambda L}\frac{\partial \mathbf{W}}{\partial r} + \mathbf{S_r}\right) = -\Lambda\mathbf{L}\frac{\partial \mathbf{W}}{\partial r} + \mathbf{LS_r} \quad \text{(A2)}$$

which gives a set of projected characteristic equations (i.e., compatibility equations). The mth row of equation (A2) reads

$$\mathbf{L_m}\frac{\partial \mathbf{W}}{\partial t} = -\lambda_m \mathbf{L_m}\frac{\partial \mathbf{W}}{\partial r} + \mathbf{L_m S_r}$$

which corresponds to the compatibility equation along the mth projected characteristic $dr/dt = \lambda_m$.

[49] According to the projected characteristic method [*Nakagawa et al.*, 1987; *Wu et al.*, 2001], the compatibility equations along the incoming waves are discarded because they do not carry any reasonable information for our physical purpose, but the information of the outgoing MHD waves is used to update the MHD variables on the boundary. In our implementation, we always suppose that $0 < v_r < v_s$ at the solar surface, just as *Hayashi* [2005] did. In this situation, three negative eigenvalues (λ_1, λ_2, and λ_3) correspond to the outgoing waves, and thus we have three compatibility equations associated with λ_1, λ_2, and λ_3 to use in prescribing the physical quantities. Up to now, two remaining constraints are required in order to accomplish the boundary treatments. Like *Hayashi* [2005], in order to stabilize the computation, the local mass flux flowing through the solar surface is limited by Ulysses observation [*Neugebauer et al.*, 2002] and v_r is assumed to be greater than a small value δv_r ($\delta v_r = 0.001$ km s^{-1}). According to the radial flow speed or solar surface mass flux $(\rho v_r)_c$ with the typical value of 5.0×10^{13} s^{-1} cm^{-2} [*Hayashi*, 2005], the two remaining constraints mentioned above are determined in the following three cases:

[50] Case I. If $0 < \rho v_r < (\rho v_r)_c$, the plasma density and pressure are assumed to be fixed

$$\frac{\partial \rho}{\partial t} = 0, \quad \frac{\partial p}{\partial t} = 0 \quad \text{(A3)}$$

[51] Case II. If $v_r < \delta v_r$, v_r is reset to be δv_r, and at the same time the adiabatic enthalpy is fixed. That is,

$$v_r = \delta v_r, \quad \frac{\partial}{\partial t}(p/\rho^\gamma) = 0 \quad \text{(A4)}$$

In practice, when $|B_r|/B$ (B is magnetic field strength) is less than some value (i.e., 0.01), this case is always implemented.

[52] Case III. If $\rho v_r > (\rho v_r)_c$, the mass flux escaping through the solar surface is settled to be the critical value $(\rho v_r)_c$, and the adiabatic enthalpy is fixed.

$$\rho v_r = (\rho v_r)_c, \quad \frac{\partial}{\partial t}(p/\rho^\gamma) = 0 \quad \text{(A5)}$$

[53] The application of one of equations (A3), (A4) and (A5), with the help of equations (4) and (7), and the three compatibility equations associated to λ_1, λ_2, and λ_3, enables us to specify the evolution of the eight physical quantities at the solar surface. So far, we have completed the description of the treatments of solar surface boundary. Actually, Case I is first applied on the whole surface to get a temporary updated version of $(v_r)_t$. Then, if $(v_r)_t$ is less than δv_r, Case II is used to update the solution variables, and if $(v_r)_t$ is greater than $(\rho v_r)_c$, Case III is employed.

Appendix B: The MHD-DUSM Results for the Remaining CRs

[54] In this appendix, we present the simulated results from the MHD-DUSM and the WSA models for the rest of the CRs (see Figures B1–B6). Meanwhile, we will also display their associated solar and the mapped interplanetary observations.

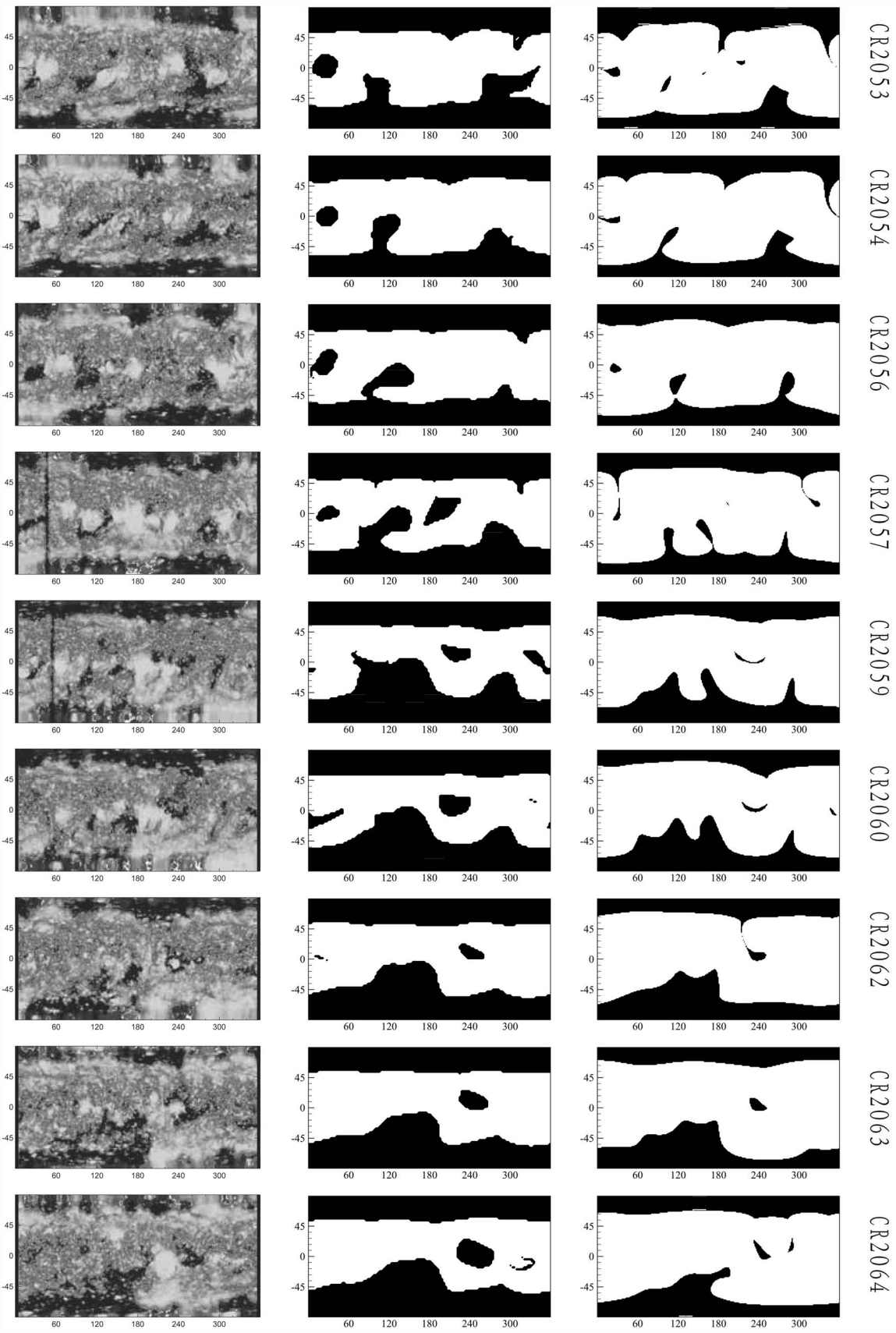

Figure B1. The same as Figure 1 but for CRs 2053, 2054, 2056, 2057, 2059, 2060, 2062, 2063, and 2064.

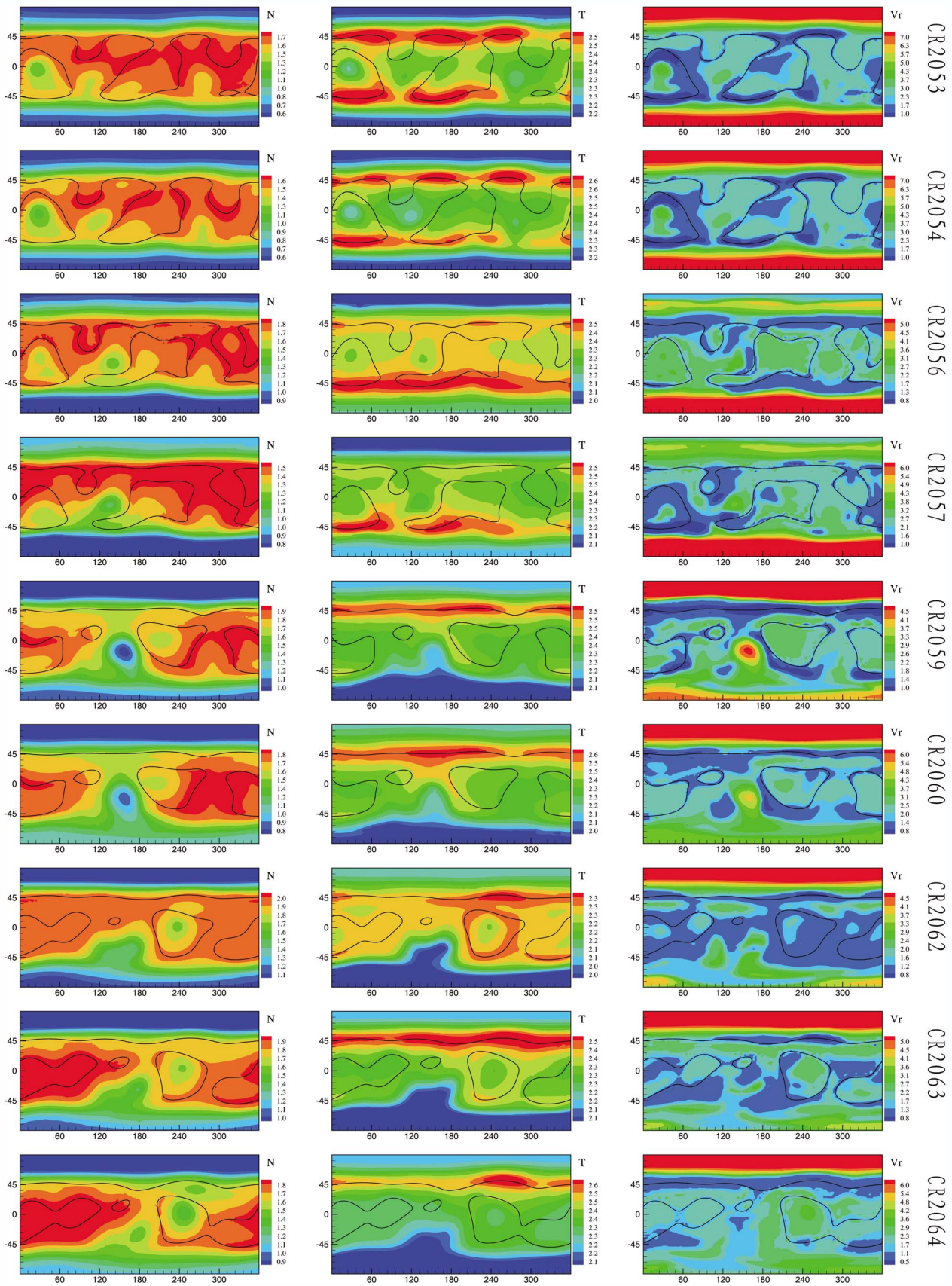

Figure B2. The same as Figure 2 but for CRs 2053, 2054, 2056, 2057, 2059, 2060, 2062, 2063, and 2064.

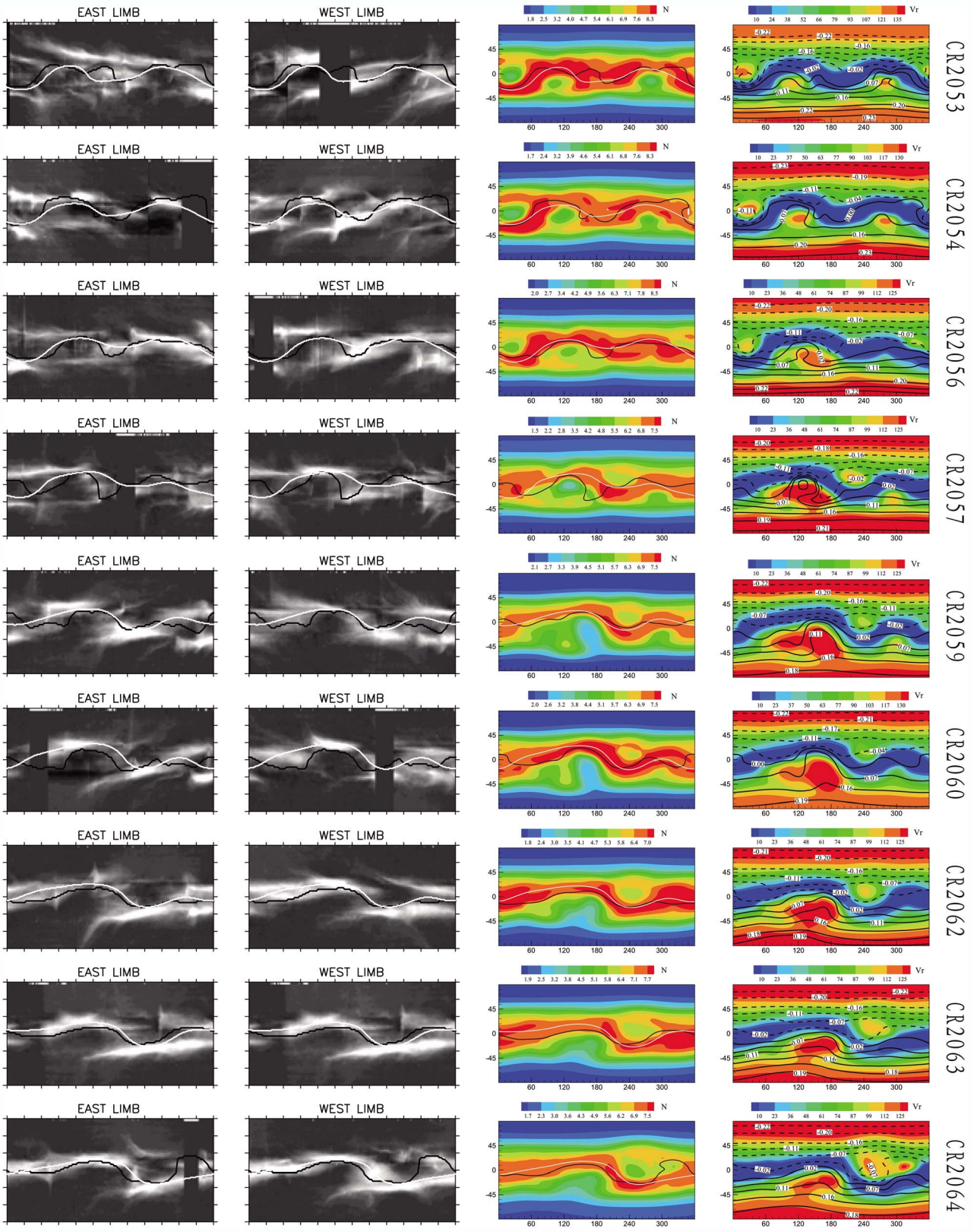

Figure B3. The same as Figure 3 but for CRs 2053, 2054, 2056, 2057, 2059, 2060, 2062, 2063, and 2064.

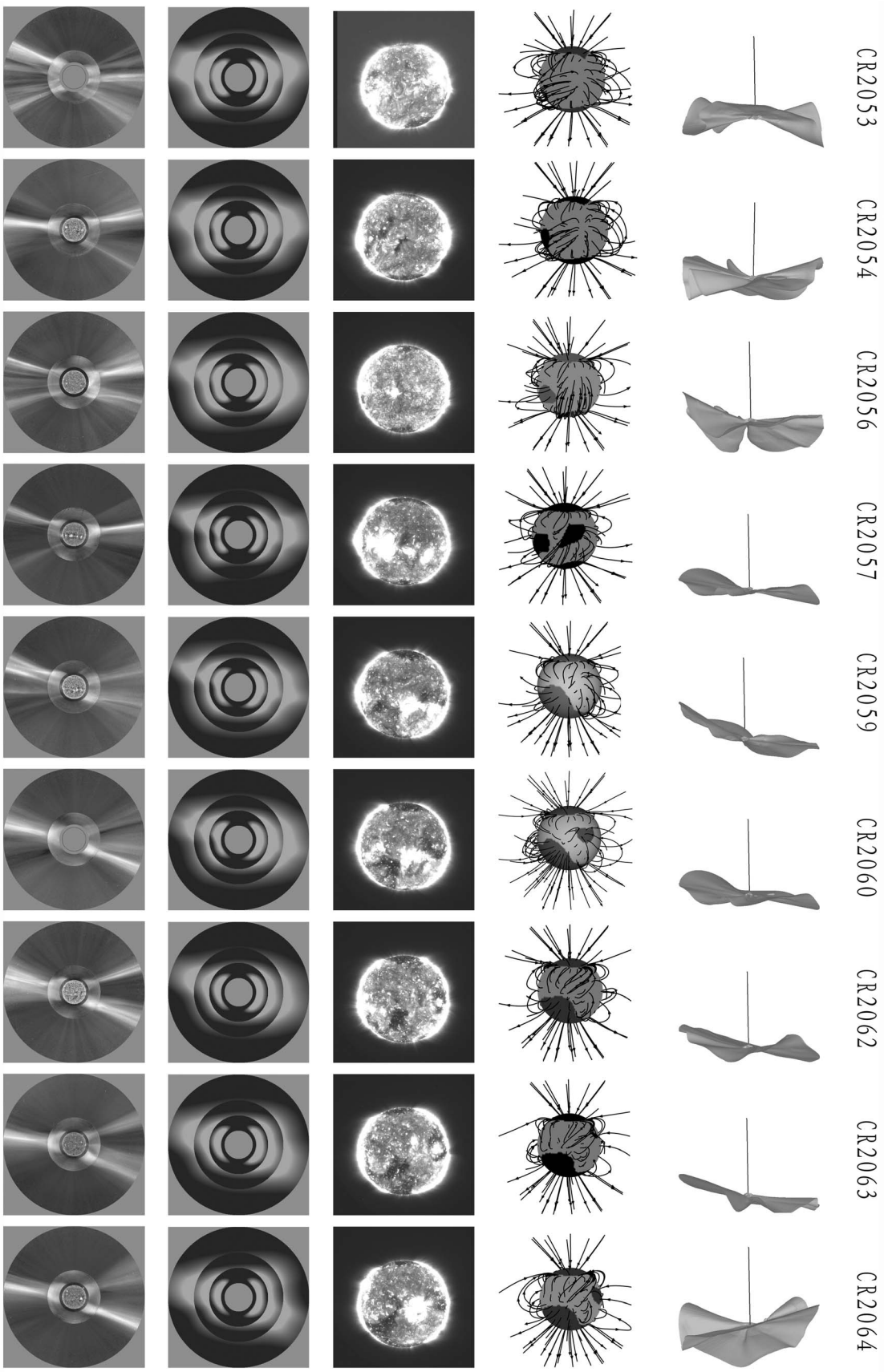

Figure B4. The same as Figure 4 but for CRs 2053, 2054, 2056, 2057, 2059, 2060, 2062, 2063, and 2064.

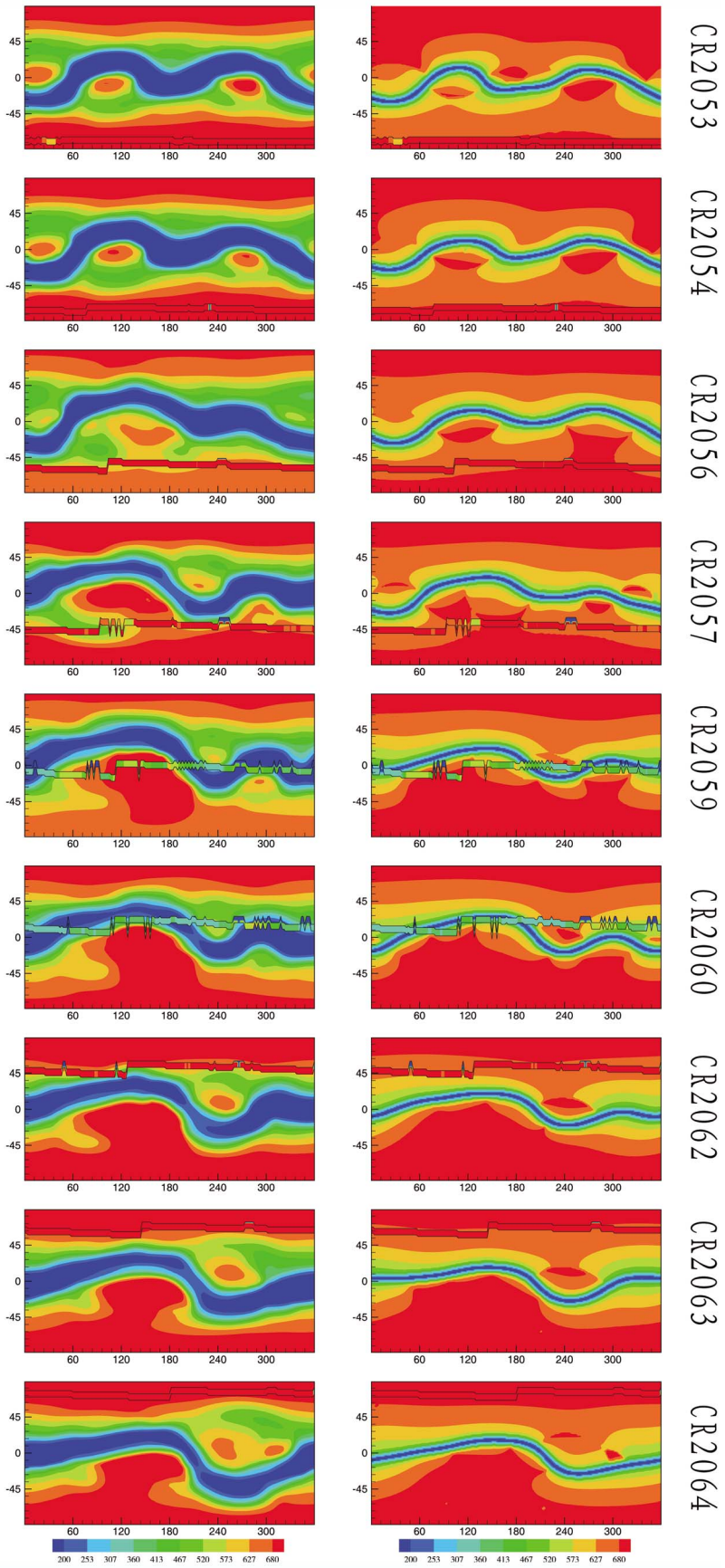

Figure B5. The same as Figure 5 but for CRs 2053, 2054, 2056, 2057, 2059, 2060, 2062, 2063, and 2064.

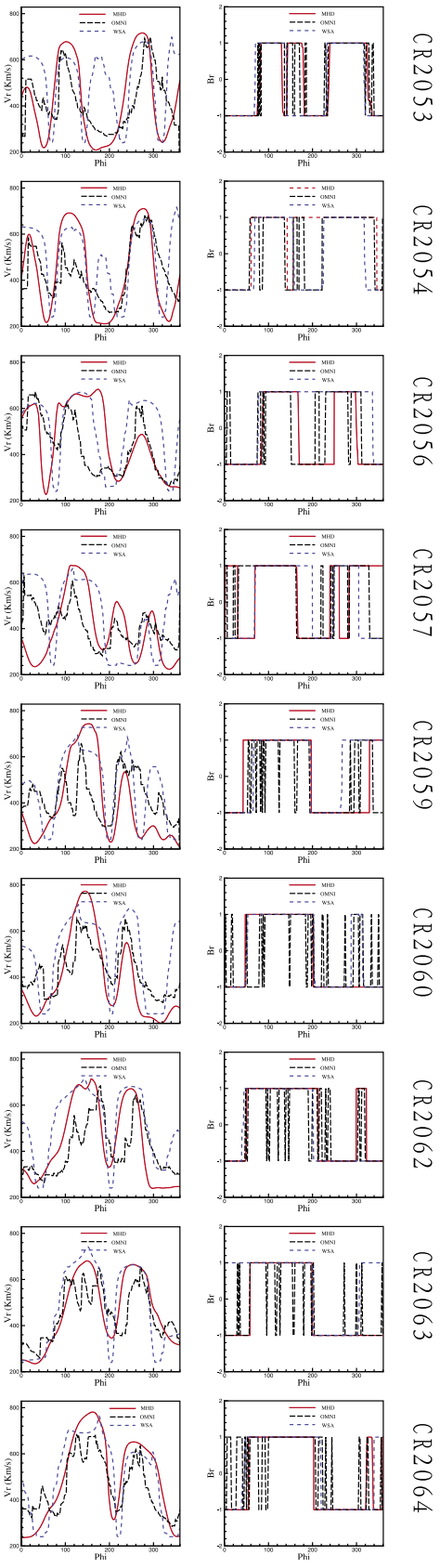

Figure B6. The same as Figure 6 but for CRs 2053, 2054, 2056, 2057, 2059, 2060, 2062, 2063, and 2064.

[55] **Acknowledgments.** This work is jointly supported by the 973 program (2012CB825601), the Chinese Academy of Sciences (KZZD-EW-01-4), the National Natural Science Foundation of China (40921063, 40890162, 41031066, 40904049, and 41004082), and the Specialized Research Fund for State Key Laboratories. The numerical calculation has been completed on our SIGMA Cluster computing system. Wilcox Solar Observatory data used in this study was obtained via the web site http://wso.stanford.edu. The Wilcox Solar Observatory is currently supported by NASA. The MLSO coronagraphs are operated by the High Altitude Observatory, which is sponsored by the National Science Foundation (USA). SOHO is a project of international cooperation between ESA and NASA. The STEREO/SECCHI data are produced by a consortium of NRL (US), LMSAL (US), NASA/GSFC (US), RAL (UK), UBHAM (UK), MPS (Germany), CSL (Belgium), IOTA (France), and IAS (France). We appreciate the SPDF COHOWeb database for helpfully providing data. The OMNI data is obtained from the GSFC/SPDF OMNIWeb interface at http://omniweb.gsfc.nasa.gov. We acknowledge the Ulysses Data System (UDS) for providing the data used in this work. Special thanks go to the anonymous reviewers for improvements of the manuscript.

[56] Philippa Browning thanks the reviewers for their assistance in evaluating this paper.

References

Abramenko, V., V. Yurchyshyn, J. Linker, Z. Mikić, J. Luhmann, and C. O. Lee (2010), Low-latitude coronal holes at the minimum of the 23rd solar cycle, *Astrophys. J.*, *712*, 813–818.

Altschuler, M. D., and G. Newkirk (1969), Magnetic fields and the structure of the solar corona. I: Methods of calculating coronal fields, *Sol. Phys.*, *9*, 131–149.

Arge, C. N., and V. J. Pizzo (2000), Improvement in the prediction of solar wind conditions using near-real time solar magnetic field updates, *J. Geophys. Res.*, *105*, 10,465–10,480.

Arge, C. N., D. Odstrcil, V. J. Pizzo, and L. R. Mayer (2003), Improved method for specifying solar wind speed near the Sun, in *Solar Wind Ten*, edited by M. Velli et al., *AIP Conf. Proc.*, *679*, 190–193.

Bumba, V., and R. Howard (1965), Large-scale distribution of solar magnetic fields, *Astrophys. J.*, *141*, 1502–1512.

Burlaga, L. F., K. W. Behannon, S. F. Hansen, G. W. Pneuman, and W. C. Feldman (1978), Sources of magnetic fields in recurrent interplanetary streams, *J. Geophys. Res.*, *83*, 4177–4185.

Chodura, R., and A. Schlueter (1981), A 3D code for MHD equilibrium and stability, *J. Comput. Phys.*, *41*, 68–88.

Cohen, O., et al. (2007), A semiempirical magnetohydrodynamical model of the solar wind, *Astrophys. J.*, *654*, L163–L166.

Cohen, O., I. V. Sokolov, I. I. Roussev, and T. I. Gombosi (2008), Validation of a synoptic solar wind model, *J. Geophys. Res.*, *113*, A03104, doi:10.1029/2007JA012797.

Contopoulos, I., C. Kalapotharakos, and M. K. Georgoulis (2011), Nonlinear force-free reconstruction of the global solar magnetic field: Methodology, *Sol. Phys.*, *269*, 351–365.

Cranmer, S. R. (2010), An efficient approximation of the coronal heating rate for use in global sun-heliosphere simulations, *Astrophys. J.*, *710*, 676–688.

Cranmer, S. R., A. A. van Ballegooijen, and R. J. Edgar (2007), Self-consistent coronal heating and solar wind acceleration from anisotropic magnetohydrodynamic turbulence, *Astrophys. J. Suppl. Ser.*, *171*, 520–551.

Dedner, A., F. Kemm, D. Kröner, C. Munz, T. Schnitzer, and M. Wesenberg (2002), Hyperbolic divergence cleaning for the MHD equations, *J. Comput. Phys.*, *175*, 645–673.

de Toma, G. (2011), Evolution of coronal holes and implications for high-speed solar wind during the minimum between cycles 23 and 24, *Sol. Phys.*, *274*, 195–217.

Downs, C., I. I. Roussev, B. van der Holst, N. Lugaz, I. V. Sokolov, and T. I. Gombosi (2010), Toward a realistic thermodynamic magnetohydrodynamic model of the global solar corona, *Astrophys. J.*, *712*, 1219–1231.

Endler, F. (1971), Interaction between the solar wind and coronal magnetic fields, PhD thesis, Göttingen University, Göttingen, Germany.

Feng, X., Y. Zhou, and S. T. Wu (2007), A novel numerical implementation for solar wind modeling by the modified conservation element/solution element method, *Astrophys. J.*, *655*, 1110–1126.

Feng, X., L. Yang, C. Xiang, S. T. Wu, Y. Zhou, and D. Zhong (2010), Three-dimensional solar wind modeling from the Sun to Earth by a SIP-CESE MHD model with a six-component grid, *Astrophys. J.*, *723*, 300–319.

Feng, X., S. Zhang, C. Xiang, L. Yang, C. Jiang, and S. T. Wu (2011a), A hybrid solar wind model of the CESE+HLL method with a Yin-Yang overset grid and an AMR grid, *Astrophys. J.*, *734*, 50, doi:10.1088/0004-637X/734/1/50.

Feng, X. S., C. Q. Xiang, and D. K. Zhong (2011b), The state-of-art of three-dimensional numerical study for corona-interplanetary process of solar storms (in Chinese), *Sci. Sin-Terrae*, *41*, 1–28.

Feng, X., L. Yang, C. Xiang, C. Jiang, X. Ma, S. Wu, D. Zhong, and Y. Zhou (2012), Validation of the 3D amr SIP-CESE solar wind model for four carrington rotations, *Sol. Phys.*, *279*, 207–229, doi:10.1007/s11207-012-9969-9.

Frazin, R. A., A. M. Vásquez, and F. Kamalabadi (2009), Quantitative, three-dimensional analysis of the global corona with multi-spacecraft differential emission measure tomography, *Astrophys. J.*, *701*, 547–560.

Grad, H., and H. Rubin (1958), Hydromagnetic equilibria and force-free fields, in *Proceedings of the Second United Nations International Conference on the Peaceful Uses of Atomic Energy*, vol. 1, pp. 190–197, U.N., Geneva, Switzerland.

Hayashi, K. (2005), Magnetohydrodynamic simulations of the solar corona and solar wind using a boundary treatment to limit solar wind mass flux, *Astrophys. J. Lett.*, *161*, 480–494.

Hayashi, K., E. Benevolenskaya, T. Hoeksema, Y. Liu, and X. P. Zhao (2006), Three-dimensional magnetohydrodynamic simulation of a global solar corona using a temperature distribution map obtained from SOHO EIT measurements, *Astrophys. J.*, *636*, L165–L168.

Hayashi, K., X. P. Zhao, and Y. Liu (2008), MHD simulations of the global solar corona around the Halloween event in 2003 using the synchronic frame format of the solar photospheric magnetic field, *J. Geophys. Res.*, *113*, A07104, doi:10.1029/2007JA012814.

Howard, R., et al. (2008), Sun Earth Connection Coronal and Heliospheric Investigation (SECCHI), *Space Sci. Rev.*, *136*, 67–115, doi:10.1007/s11214-008-9341-4.

Hu, Y. Q., X. S. Feng, S. T. Wu, and W. B. Song (2008), Three-dimensional MHD modeling of the global corona throughout solar cycle 23, *J. Geophys. Res.*, *113*, A03106, doi:10.1029/2007JA012750.

Jiang, C., X. Feng, J. Zhang, and D. Zhong (2010), AMR simulations of magnetohydrodynamic problems by the CESE method in curvilinear coordinates, *Sol. Phys.*, *267*, 463–491.

Judge, P. G. (1998), Spectral lines for polarization measurements of the coronal magnetic field. I. Theoretical intensities, *Astrophys. J.*, *500*, 1009, doi:10.1086/305775.

Kilpua, E. K. J., et al. (2009), Small solar wind transients and their connection to the large-scale coronal structure, *Sol. Phys.*, *256*, 327–344.

Klimchuk, J. A. (2006), On solving the coronal heating problem, *Sol. Phys.*, *234*, 41–77.

Lai, M.-C., and W.-C. Wang (2002), Fast direct solvers for Poisson equation on 2D polar and spherical geometries, *Numer. Methods Partial Differential Equations*, *18*, 56–68.

Lepri, S. T., S. K. Antiochos, P. Riley, L. Zhao, and T. H. Zurbuchen (2008), Comparison of heliospheric in situ data with the quasi-steady solar wind models, *Astrophys. J.*, *674*, 1158–1166.

Lin, H., M. J. Penn, and S. Tomczyk (2000), A new precise measurement of the coronal magnetic field strength, *Astrophys. J.*, *541*, L83–L86.

Linker, J. A., et al. (1999), Magnetohydrodynamic modeling of the solar corona during Whole Sun Month, *J. Geophys. Res.*, *104*, 9809–9830.

Lionello, R., J. A. Linker, Z. Mikić, and P. Riley (2006), The latitudinal excursion of coronal magnetic field lines in response to differential rotation: MHD simulations, *Astrophys. J.*, *642*, L69–L72.

Lionello, R., J. A. Linker, and Z. Mikić (2009), Multispectral emission of the Sun during the first whole Sun month: Magnetohydrodynamic simulations, *Astrophys. J.*, *690*, 902–912.

Liu, Y., J. T. Hoeksema, X. Zhao, and R. M. Larson (2007), MDI synoptic charts of magnetic field: Interpolation of polar fields, *Bull. Am. Astron. Soc.*, *38*, 129.

Luhmann, J. G., Y. Li, C. N. Arge, P. R. Gazis, and R. Ulrich (2002), Solar cycle changes in coronal holes and space weather cycles, *J. Geophys. Res.*, *107*(A8), 1154, doi:10.1029/2001JA007550.

Luhmann, J. G., C. O. Lee, Y. Li, C. N. Arge, A. B. Galvin, K. Simunac, C. T. Russell, R. A. Howard, and G. Petrie (2009), Solar wind sources in the late declining phase of cycle 23: Effects of the weak solar polar field on high speed streams, *Sol. Phys.*, *256*, 285–305.

MacNeice, P., K. M. Olson, C. Mobarry, R. de Fainchtein, and C. Packer (2000), PARAMESH: A parallel adaptive mesh refinement community toolkit, *Comput. Phys. Commun.*, *126*, 330–354.

Marder, B. (1987), A method for incorporating Gauss' law into electromagnetic PIC codes, *J. Comput. Phys.*, *68*, 48–55.

McGregor, S. L., W. J. Hughes, C. N. Arge, and M. J. Owens (2008), Analysis of the magnetic field discontinuity at the potential field source surface and Schatten Current Sheet interface in the Wang–Sheeley–Arge model, *J. Geophys. Res.*, *113*, A08112, doi:10.1029/2007JA012330.

McGregor, S. L., W. J. Hughes, C. N. Arge, D. Odstrcil, and N. A. Schwadron (2011a), The radial evolution of solar wind speeds, *J. Geophys. Res.*, *116*, A03106, doi:10.1029/2010JA016006.

McGregor, S. L., W. J. Hughes, C. N. Arge, M. J. Owens, and D. Odstrcil (2011b), The distribution of solar wind speeds during solar minimum: Calibration for numerical solar wind modeling constraints on the source of the slow solar wind, *J. Geophys. Res.*, *116*, A03101, doi:10.1029/2010JA015881.

Mignone, A., and P. Tzeferacos (2010), A second-order unsplit Godunov scheme for cell-centered MHD: The CTU-GLM scheme, *J. Comput. Phys.*, *229*, 2117–2138.

Mikić, Z., and A. N. McClymont (1994), Deducing coronal magnetic fields from vector magnetograms, in *Solar Active Region Evolution: Comparing Models With Observations*, edited by K. S. Balasubramaniam and G. W. Simon, *Astron. Soc. Pac. Conf. Ser.*, *68*, 225.

Mikić, Z., J. A. Linker, D. D. Schnack, R. Lionello, and A. Tarditi (1999), Magnetohydrodynamic modeling of the global solar corona, *Phys. Plasmas*, *6*, 2217–2224.

Nakagawa, Y. (1974), Dynamics of the solar magnetic field. I. Method of examination of force-free magnetic fields, *Astrophys. J.*, *190*, 437–440.

Nakagawa, Y. (1980), Evolution of solar magnetic fields: A new approach to MHD initial-boundary value problems by the method of near characteristics, *Astrophys. J.*, *240*, 275–299.

Nakagawa, Y. (1981a), Evolution of magnetic field and atmospheric response. I. Three-dimensional formulation by the method of projected characteristics, *Astrophys. J.*, *247*, 707–718.

Nakagawa, Y. (1981b), Evolution of magnetic field and atmospheric responses. II. Formulation of proper boundary equations, *Astrophys. J.*, *247*, 719–733.

Nakagawa, Y., Y. Q. Hu, and S. T. Wu (1987), The method of projected characteristics for the evolution of magnetic arches, *Astron. Astrophys.*, *179*, 354–370.

Nakamizo, A., T. Tanaka, Y. Kubo, S. Kamei, H. Shimazu, and H. Shinagawa (2009), Development of the 3-D MHD model of the solar corona-solar wind combining system, *J. Geophys. Res.*, *114*, A07109, doi:10.1029/2008JA013844.

Neugebauer, M., et al. (1998), Spatial structure of the solar wind and comparisons with solar data and models, *J. Geophys. Res.*, *103*, 14,587–14,600.

Neugebauer, M., P. C. Liewer, E. J. Smith, R. M. Skoug, and T. H. Zurbuchen (2002), Sources of the solar wind at solar activity maximum, *J. Geophys. Res.*, *107*(A12), 1488, doi:10.1029/2001JA000306.

Olson, K. (2006), PARAMESH: A parallel adaptive grid tool, in *Parallel Computational Fluid Dynamics 2005: Theory and Applications*, pp. 341–348, Elsevier, New York.

Owens, M. J., C. N. Arge, H. E. Spence, and A. Pembroke (2005), An event-based approach to validating solar wind speed predictions: High-speed enhancements in the Wang-Sheeley-Arge model, *J. Geophys. Res.*, *110*, A12105, doi:10.1029/2005JA011343.

Owens, M. J., H. E. Spence, S. McGregor, W. J. Hughes, J. M. Quinn, C. N. Arge, P. Riley, J. Linker, and D. Odstrcil (2008), Metrics for solar wind prediction models: Comparison of empirical, hybrid, and physics-based schemes with 8 years of L1 observations, *Space Weather*, *6*, S08001, doi:10.1029/2007SW000380.

Parker, E. N. (1963), *Interplanetary Dynamical Processes*, Interscience, New York.

Petrie, G. J. D., and I. Patrikeeva (2009), A comparative study of magnetic fields in the solar photosphere and chromosphere at equatorial and polar latitudes, *Astrophys. J.*, *699*, 871–884.

Petrie, G. J. D., J. Bolding, R. Clark, K. Donaldson-Hanna, J. W. Harvey, F. Hill, C. Toner, and T. M. Wentzel (2008), GONG synoptic magnetogram program: Near-real-time coronal magnetic field model, in *Subsurface and Atmospheric Influences on Solar Activity*, edited by R. Howe et al., *Astron. Soc. Pac. Conf. Ser.*, *383*, 181–190.

Pneuman, G. W., and R. A. Kopp (1971), Gas-magnetic field interactions in the solar corona, *Sol. Phys.*, *18*, 258–270.

Powell, K. G., P. L. Roe, T. J. Linde, T. I. Gombosi, and D. L. de Zeeuw (1999), A solution-adaptive upwind scheme for ideal magnetohydrodynamics, *J. Comput. Phys.*, *154*, 284–309.

Riley, P., and J. G. Luhmann (2012), Interplanetary signatures of unipolar streamers and the origin of the slow solar wind, *Sol. Phys.*, *277*, 355–373.

Riley, P., J. A. Linker, and Z. Mikić (2001), An empirically-driven global MHD model of the solar corona and inner heliosphere, *J. Geophys. Res.*, *15*,889–15,902.

Riley, P., J. A. Linker, Z. Mikić, R. Lionello, S. A. Ledvina, and J. G. Luhmann (2006), A comparison between global solar magnetohydrodynamic and potential field source surface model results, *Astrophys. J.*, *653*, 1510–1516.

Roussev, I. I., T. G. Forbes, T. I. Gombosi, I. V. Sokolov, D. L. DeZeeuw, and J. Birn (2003), A three-dimensional flux rope model for coronal mass ejections based on a loss of equilibrium, *Astrophys. J.*, *588*, L45–L48.

Ruan, P., T. Wiegelmann, B. Inhester, T. Neukirch, S. K. Solanki, and L. Feng (2008), A first step in reconstructing the solar corona self-consistently

with a magnetohydrostatic model during solar activity minimum, *Astron. Astrophys.*, *481*, 827–834.
Sakurai, T. (1981), Calculation of force-free magnetic field with non-constant α, *Sol. Phys.*, *69*, 343–359, doi:10.1007/BF00149999.
Schatten, K. H. (1971), Current sheet magnetic model for the solar corona, *Cosmic Electrodyn.*, *2*, 232–245.
Schatten, K. H., J. M. Wilcox, and N. F. Ness (1969), A model of interplanetary and coronal magnetic fields, *Sol. Phys.*, *6*, 442–455.
Schrijver, C. J., and M. L. De Rosa (2003), Photospheric and heliospheric magnetic fields, *Sol. Phys.*, *212*, 165–200.
Smith, S. M., and K. H. Schatten (1970), Preliminary comparison of predicted and observed structure of the solar corona at the eclipse of 7 March 1970, *Bull. Am. Astron. Soc.*, *2*, 345.
Song, M. T., C. Fang, Y. H. Tang, S. T. Wu, and Y. A. Zhang (2006), A new and fast way to reconstruct a nonlinear force-free field in the solar corona, *Astrophys. J.*, *649*, 1084, doi:10.1086/506249.
Song, M. T., C. Fang, H. Q. Zhang, Y. H. Tang, S. T. Wu, and Y. A. Zhang (2007), Reconstructing spherical nonlinear force-free field in the solar corona, *Astrophys. J.*, *666*, 491–500.
Song, W. M., X. J. Zhang, Y. Wang, and X. Y. Ren (1999), The perfect project theorem for a vector function on vector wave function space, *Chin. J. Radio Sci.*, *14*, 247–253.
Sun, X., Y. Liu, J. T. Hoeksema, K. Hayashi, and X. Zhao (2011), A new method for polar field interpolation, *Sol. Phys.*, *270*, 9–22.
Svalgaard, L., T. L. Duvall Jr., and P. H. Scherrer (1978), The strength of the Sun's polar fields, *Sol. Phys.*, *58*, 225–239.
Tokumaru, M., M. Kojima, and K. Fujiki (2010), Solar cycle evolution of the solar wind speed distribution from 1985 to 2008, *J. Geophys. Res.*, *115*, A04102, doi:10.1029/2009JA014628.
Tomczyk, S., et al. (2008), An instrument to measure coronal emission line polarization, *Sol. Phys.*, *247*, 411–428.
Tripathi, D., H. E. Mason, and J. A. Klimchuk (2010), Evidence of impulsive heating in active region core loops, *Astrophys. J.*, *723*, 713–718.
Usmanov, A. V. (1993), A global numerical 3-D MHD model of the solar wind, *Sol. Phys.*, *146*, 377–396.
van Ballegooijen, A. A., M. Asgari-Targhi, S. R. Cranmer, and E. E. DeLuca (2011), Heating of the solar chromosphere and corona by Alfvén wave turbulence, *Astrophys. J.*, *736*, 3, doi:10.1088/0004-637X/736/1/3.
van der Holst, B., W. B. Manchester, R. A. Frazin, A. M. Vásquez, G. Tóth, and T. I. Gombosi (2010), A data-driven, two-temperature solar wind model with Alfvén waves, *Astrophys. J.*, *725*, 1373–1383.
Vásquez, A. M., R. A. Frazin, and W. B. Manchester IV (2010), The solar minimum corona from differential emission measure tomography, *Astrophys. J.*, *715*, 1352–1365.
Wang, A. H., S. T. Wu, E. Tandberg-Hanssen, and F. Hill (2011), Utilization of multiple measurements for global three-dimensional magnetohydrodynamic simulations, *Astrophys. J.*, *732*, 19–31.
Wang, S., Y. Hu, and S. T. Wu (1982), Full-implicit continuous Eulerian scheme in the spherical coordinates and its applications to solar phenomena, *Sci. Sin., Ser. A, Math. Phys. Astron. Tech. Sci.*, *25*, 1305–1318.
Wang, Y.-M. (1996), Nonradial coronal streamers, *Astrophys. J. Lett.*, *456*, L119.
Wang, Y.-M., and N. R. Sheeley Jr. (1988), The solar origin of long-term variations of the interplanetary magnetic field strength, *J. Geophys. Res.*, *93*, 11,227–11,236.
Wang, Y.-M., and N. R. Sheeley Jr. (1992), On potential field models of the solar corona, *Astrophys. J.*, *392*, 310–319.
Wang, Y.-M., et al. (1997), Origin and evolution of coronal streamer structure during the 1996 minimum activity phase, *Astrophys. J.*, *485*, 875, doi:10.1086/304467.
Wang, Y.-M., N. R. Sheeley, and N. B. Rich (2000), Evolution of coronal streamer structure during the rising phase of solar cycle 23, *Geophys. Res. Lett.*, *27*, 149–152.
Wang, Y.-M., N. R. Sheeley, and M. D. Andrews (2002), Polarity reversal of the solar magnetic field during cycle 23, *J. Geophys. Res.*, *107*(A12), 1465, doi:10.1029/2002JA009463.
Wang, Y.-M., N. R. Sheeley, Jr., and N. B. Rich (2007), Coronal pseudostreamers, *Astrophys. J.*, *658*, 1340–1348.
Wang, Y.-M., E. Robbrecht, and N. R. Sheeley Jr. (2009), On the weakening of the polar magnetic fields during solar cycle 23, *Astrophys. J.*, *707*, 1372–1386.
Wei, F., X. Feng, H. Cai, and Q. Zhou (2003), Global distribution of coronal mass outputs and its relation to solar magnetic field structures, *J. Geophys. Res.*, *108* (A6), 1238, doi:10.1029/2002JA009439.
Wheatland, M. S., P. A. Sturrock, and G. Roumeliotis (2000), An optimization approach to reconstructing force-free fields, *Astrophys. J.*, *540*, 1150, doi:10.1086/309355.
Wiegelmann, T. (2007), Computing nonlinear force-free coronal magnetic fields in spherical geometry, *Sol. Phys.*, *240*, 227–239, 10.1007/s11207-006-0266-3.
Wiegelmann, T. (2008), Nonlinear force-free modeling of the solar coronal magnetic field, *J. Geophys. Res.*, *113*, A03S02, doi:10.1029/2007JA012432.
Wu, S. T., and J. F. Wang (1987), Numerical tests of a modified full implicit continuous Eulerian (FICE) scheme with projected normal characteristic boundary conditions for MHD flows, *Comput. Methods Appl. Mech. Eng.*, *64*, 267–282.
Wu, S. T., H. M. Chang, and M. J. Hagyard (1985), On the numerical computation of nonlinear force-free magnetic fields, *NASA Conf. Publ.*, *2374*, 17–48.
Wu, S. T., M. T. Sun, H. M. Chang, M. J. Hagyard, and G. A. Gary (1990a), On the numerical computation of nonlinear force-free magnetic fields, *Astrophys. J.*, *362*, 698–708.
Wu, S. T., M. T. Sun, and T. Sakurai (1990b), A comparison between progressive extension method (PEM) and iterative method (IM) for magnetic field extrapolations in the solar atmosphere, *memsai*, *61*, 477–484.
Wu, S. T., H. Zheng, S. Wang, B. J. Thompson, S. P. Plunkett, X. P. Zhao, and M. Dryer (2001), Three-dimensional numerical simulation of MHD waves observed by the Extreme Ultraviolet Imaging Telescope, *J. Geophys. Res.*, *106*, 25,089–25,102.
Wu, S. T., A. H. Wang, Y. Liu, and J. T. Hoeksema (2006), Data-driven magnetohydrodynamic model for active region evolution, *Astrophys. J.*, *652*, 800–811.
Wu, S. T., A. H. Wang, G. A. Gary, A. Kucera, J. Rybak, Y. Liu, B. Vršnak, and V. Yurchyshyn (2009), Analyses of magnetic field structures for active region 10720 using a data-driven 3D MHD model, *Adv. Space Res.*, *44*, 46–53.
Yan, Y., and Z. Li (2006), Direct boundary integral formulation for solar non-constant-α force-free magnetic fields, *Astrophys. J.*, *638*, 1162–1168.
Yan, Y., and T. Sakurai (2000), New boundary integral equation representation for finite energy force-free magnetic fields in open space above the Sun, *Sol. Phys.*, *195*, 89–109, doi:10.1023/A:1005248128673.
Yang, L., X. Feng, C. Xiang, and C. Jiang (2011), Numerical validation and comparison of three solar wind heating methods by the SIP-CESE MHD model, *Chin. Phys. Lett.*, *28*, 039601, doi:10.1088/0256-307X/28/3/039601.
Yeates, A. R., and D. H. Mackay (2009), Modelling the global solar corona: III. Origin of the hemispheric pattern of filaments, *Sol. Phys.*, *254*, 77–88.
Yeates, A. R., D. H. Mackay, and A. A. van Ballegooijen (2007), Modelling the global solar corona: Filament chirality observations and surface simulations, *Sol. Phys.*, *245*, 87–107.
Yeates, A. R., D. H. Mackay, and A. A. van Ballegooijen (2008), Modelling the global solar corona II: Coronal evolution and filament chirality comparison, *Sol. Phys.*, *247*, 103–121.
Yeates, A. R., D. H. Mackay, A. A. van Ballegooijen, and J. A. Constable (2010), A nonpotential model for the Sun's open magnetic flux, *J. Geophys. Res.*, *115*, A09112, doi:10.1029/2010JA015611.
Yeh, T., and M. Dryer (1985), A constraint on boundary data for magnetic solenoidality in MHD calculations, *Astrophys. Space Sci.*, *117*, 165–171.
Zhao, X., and J. T. Hoeksema (1994), A coronal magnetic field model with horizontal volume and sheet currents, *Sol. Phys.*, *151*, 91–105.
Zhao, X., and J. T. Hoeksema (1995), Prediction of the interplanetary magnetic field strength, *J. Geophys. Res.*, *100*, 19–33.
Zhao, X. P., and J. T. Hoeksema (2010), The magnetic field at the inner boundary of the heliosphere around solar minimum, *Sola. Phys.*, *266*, 379–390.